INL/EXT-16-40059 Rev. 0

September 2016

Behavior of U_3Si_2 Fuel and FeCrAl Cladding under Normal Operating and Accident Reactor Conditions

K. A. Gamble
J. D. Hales
G. Pastore
T. Barani
D. Pizzocri

with contributions from

Argonne National Laboratory
Idaho National Laboratory
Los Alamos National Laboratory
University of Tennessee, Knoxville

INL/EXT-16-40059 Rev. 0

Behavior of U_3Si_2 Fuel and FeCrAl Cladding under Normal Operating and Accident Reactor Conditions

K. A. Gamble[1]
J. D. Hales[1]
G. Pastore[1]
T. Barani[1]
D. Pizzocri[1]

with contributions from

Argonne National Laboratory
Idaho National Laboratory
Los Alamos National Laboratory
University of Tennessee, Knoxville

September 2016

[1]Idaho National Laboratory
Fuel Modeling and Simulation Department
Idaho Falls, Idaho 83415

Prepared for the
U.S. Department of Energy
Office of Nuclear Energy
Under U.S. Department of Energy-Idaho Operations Office
Contract DE-AC07-99ID13727

Abstract

As part of the Department of Energy's Nuclear Energy Advanced Modeling and Simulation program, an Accident Tolerant Fuel High Impact Problem was initiated at the beginning of fiscal year 2015 to investigate the behavior of U_3Si_2 fuel and iron-chromium-aluminum (FeCrAl) cladding under normal operating and accident reactor conditions. The High Impact Problem was created in response to the United States Department of Energy's renewed interest in accident tolerant materials after the events that occurred at the Fukushima Daiichi Nuclear Power Plant in 2011. The High Impact Problem is a multinational laboratory and university collaborative research effort between Idaho National Laboratory, Los Alamos National Laboratory, Argonne National Laboratory, and the University of Tennessee, Knoxville. This report primarily focuses on the engineering scale research in fiscal year 2016 with brief summaries of the lower length scale developments in the areas of density functional theory, cluster dynamics, rate theory, and phase field being presented.

Contents

1 Introduction

In March 2011, a magnitude 9.0 earthquake struck off the coast of Japan. The earthquake and the associated tsunami resulted in tens of thousands of deaths, hundreds of thousands of damaged buildings, and a cost estimated to be in the hundreds of millions of dollars.

One consequence of the tsunami was the flooding of backup power generators at the Fukushima Daiichi Nuclear Power Station. The loss of power to coolant systems led to high temperatures, oxidation of Zr-based alloys, hydrogen production, melted fuel, and hydrogen explosions. As a result, a massive cleanup effort is underway at Fukushima Daiichi. The economic impacts, both those directly related to the cleanup and those affecting the nuclear energy sector generally, are significant.

Following the disaster, efforts to develop nuclear fuels with enhanced accident tolerance were begun by many nations, corporations, and research institutes. In the United States, the Department of Energy's Office of Nuclear Energy accelerated research on this topic as part of its Fuel Cycle Research and Development (FCRD) Advanced Fuels Campaign (AFC). One product of this work is Light Water Reactor Accident Tolerant Fuel Performance Metrics [1], a report by AFC that outlines a set of metrics that can be used to guide selection of promising accident tolerant fuel (ATF) concepts. Since that time, the AFC has begun irradiation of several ATF materials in Idaho National Laboratory's Advanced Test Reactor. The most promising ATF concepts are receiving increased focus and research funding. This work aims to prepare one or more candidate fuels for insertion in a commercial reactor as a lead test rod or lead test assembly in 2022.

Given the aggressive development schedule, it is impossible to perform a comprehensive set of experiments to provide material characterization data. Therefore, the AFC plans to utilize computational analysis tools in an effort to understand the proposed materials.

The Nuclear Energy Advanced Modeling and Simulation (NEAMS) program in DOE has for some time been developing computational analysis tools. These include BISON [2–4] and Marmot [5], analysis tools tailored to nuclear fuel at the engineering scale and grain scale, respectively. Recently, NEAMS has introduced what it calls High Impact Problems (HIPs) into its program plan. These HIPs are intended to make a significant advance in a particular area of nuclear power research in a short period of time (3 years or less). NEAMS has chosen an ATF project, which emphasizes utilizing BISON and Marmot to model proposed materials, as its first HIP. This report focuses on the multiscale and multiphysics developments of ATF fuel concepts through the ATF HIP. Participating national laboratories include Idaho National Laboratory (INL), Los Alamos National Laboratory (LANL), and Argonne National Laboratory (ANL). Contributions are also being made by university researchers, including at the University of Tennessee, Knoxville.

Accident tolerant fuels are expected to give similar or better performance during normal operation and improved performance in accident scenarios. Improved performance in accidents has been interpreted to mean increasing the coping time available to reactor operators. That is, an accident tolerant fuel will allow more time for cooling to be applied before unacceptable oxidation or melting occurs.

Of the many accident tolerant fuel concepts, two are the main focus of the NEAMS ATF HIP: uranium silicide (U_3Si_2) fuel and iron-chromium-aluminum (FeCrAl) cladding. These were chosen through consultation with the Advanced Fuels Campaign as leading concepts, those seen as having a reasonable likelihood of being placed in a commercial reactor in the 2022 time frame. U_3Si_2 is promising due to its higher thermal conductivity, which will give lower fuel temperatures during normal operation, and its higher uranium density, which has economic benefits. FeCrAl is promising due to a low oxidation rate and high strength.

The remainder of this report reviews insight related to U_3Si_2 and FeCrAl concepts. A brief overview of the concepts comes first. Next is a set of overviews of research at lower length scales in support of the engineering scale model development. Key contributors to each overview are listed. Next comes details of engineering scale models and analysis, including normal operation and accident behavior. The report closes with a summary and list of possible future work.

2 Overview of ATF Concepts

This chapter briefly introduces the two ATF candidates that are the focus of the NEAMS ATF HIP: U_3Si_2 fuel and FeCrAl cladding.

2.1 U_3Si_2

U_3Si_2 as a replacement for UO_2 is being explored by the Advanced Fuels Campaign and Westinghouse.

2.1.1 Advantages

A main advantage of U_3Si_2 over UO_2 fuel is the higher thermal conductivity. Thermal conductivity of UO_2 is ~2-5 W/m/K whereas the thermal conductivity of U_3Si_2 is ~15-30 W/m/K. This large difference results in lower fuel centerline temperatures and lower temperature gradients in the fuel pellet. Lower temperature gradients lower the likelihood of pellet cracking and relocation.

The high uranium density of U_3Si_2 (11.3 g-U/cm^3 versus 9.7 g-U/cm^3 for UO_2 [6]) is economically attractive since it may enable higher burnup and longer cycle length. Uranium nitride fuel is attractive for the same reason, but its poor performance in water precludes its use without being combined with another material, such as U_3Si_2.

2.1.2 Disadvantages

Early work indicates that U_3Si_2 is more susceptible to chemical reaction than is UO_2. For example, Harp et al. [7] report a “layered structure of corrosion products” on the surface of U_3Si_2 subjected to contact with water at 300°C for up to 24 hours. Furthermore, the authors report interdiffusion of U_3Si_2 and Zircaloy when tested at 800°C for 100 hours. Fe and Cr phases formed at the interface, with $ZrSi_2$ and U-rich areas in Zircaloy also present. The authors indicate that further studies are needed, but it is clear that U_3Si_2 is more active than UO_2.

An exploration of increasing the oxidation resistance of U_3Si_2 was the subject of the study by Wood et al. [8]. Oxidation in 400°C air was shown to improve with the addition of aluminum. However, any alloying element decreases the uranium content per volume, diminishing the high uranium density advantage of the fuel. Oxidation of U_3Si_2 is further explored in [9].

Production of U_3Si_2 pellets has been completed in sufficient quantities to load experiments for irradiation in the Advanced Test Reactor. Scaling up the process to enable fueling whole assemblies and reactors remains to be done, with challenges still to be met [10].

2.1.3 Unknowns

Swelling of U_3Si_2 is a subject of some concern. Finlay et al. [11] reported significant swelling of U_3Si_2 under irradiation, and that data was used by Metzger et al. [12] to develop the first U_3Si_2 swelling model in BISON. The swelling in that model is quadratic in nature, giving significant swelling after a certain burnup. If the model is accurate, the swelling will induce high compressive stress in the fuel pellets. The effects of those stresses are unknown but could potentially involve pellet damage, particularly at the pellet edge where burnup is highest.

However, Finlay et al. attribute the high swelling to a change from a crystalline to an amorphous state. This change may not occur at reactor temperatures, and therefore the swelling may be considerably lower than originally assumed. More research, both experimental and computational, is underway to understand the phenomenon better.

Fuel swelling is connected to fission gas release, and just as there is uncertainty about swelling, there is uncertainty about the amount of fission gas that will be released from U_3Si_2 fuel. Experimental evidence is missing in this respect, and there is a need for experimental and theoretical work on fission gas behavior in U_3Si_2.

2.2 FeCrAl

Iron-chromium-aluminum alloy (FeCrAl) has been proposed as a cladding material to replace Zircaloy. This concept is being pursued by the Advanced Fuels Campaign and General Electric.

2.2.1 Advantages

One of the most significant factors in the Fukushima Daiichi power plant accident was the oxidation of Zircaloy. Given that fact, perhaps the most attractive characteristic of FeCrAl cladding is its low oxidation rate. Oxidation rates for FeCrAl are approximately 1000 times lower than the oxidation rates of Zircaloy [13, 14]. The oxidation rates for FeCrAl are so low that a good approximation when modeling is that the FeCrAl cladding will not oxidize at all.

The stiffness of FeCrAl is roughly twice that of Zircaloy [14], while the yield stress is higher by a factor of four [13].

2.2.2 Disadvantages

The thermal neutron absorption cross section of FeCrAl is about ten times that of Zircaloy. This neutronic penalty necessitates thinner cladding, which is possible due to the higher strength of FeCrAl. However, thinner cladding, including the use of slightly larger pellets giving the same cold gap width, is not enough to compensate for the neutronic penalty. Enriching the fuel beyond the current 5% limit appears to be necessary [14].

Current estimates are that FeCrAl cladding, with its neutronic penalty, will impose a fuel cost increase of 15-35% [13, 14].

A second disadvantage of FeCrAl cladding is the anticipated increase in tritium release to the coolant. The permeability of hydrogen in FeCrAl is about 100 times higher than its permeability in Zircaloy [15]. Mitigation strategies for this weakness are being considered.

2.2.3 Unknowns

Material data for FeCrAl under irradiation is just now becoming available. While reasonable expectations have been stated for the irradiation behavior, more testing is necessary to confirm the assumptions.

The thermal creep rate of FeCrAl is significantly lower than that of Ziracloy. A preliminary correlation for irradiation creep is available, and further experimental investigations are currently underway at Halden. It is also worth considering the possibility of using the creep rate as a design parameter. Perhaps slight alloying adjustments might be made that result in a creep rate that optimizes a particular behavior of the cladding.

Isotropic swelling of FeCrAl alloys under fast neutron flux is not yet characterized.

It is expected that FeCrAl will become harder and more brittle with irradiation [14]. The extent of the changes will have important consequences for the accident behavior of the cladding. Recent work indicates that burst FeCrAl tubes may open more fully than Zircaloy tubes [16]. It is possible that an embrittled cladding would open even more fully upon burst, increasing the likelihood of fuel being dispersed into the coolant.

2.3 Other concepts

Several other accident tolerant fuel concepts have been proposed. While not a primary focus of the ATF HIP, a few are mentioned here.

Silicon carbide cladding is being proposed due to low oxidation rates. However, challenges include dissolution in coolant [17], manufacturing and maintaining hermiticity [18], and joining [19].

Coated Zircaloy cladding is another possibility. This technology is being pursued by several institutions, including AREVA [20]. Challenges include manufacturing and the fact that initial work has focused on the exterior of the cladding, leaving the interior of the cladding unprotected.

Fully ceramic microencapsulated (FCM) fuel has also been proposed (see [21] as an example). The FCM concept involves TRISO fuel particles embedded in a matrix, the whole taking on a geometry similar to that of UO_2 pellets. FCM, like other accident tolerant fuel concepts, lacks detailed irradiated material behavior data and is likely to be more expensive than the current UO_2/Zircaloy fuel system.

3 Lower Length Scale Developments

The bulk of this report focuses on engineering scale analysis of ATF concepts. In support of the engineering scale work, significant lower length scale efforts are underway at Argonne National Laboratory, Idaho National Laboratory, Los Alamos National Laboratory, and the University of Tennessee, Knoxville. This chapter reviews this lower length scale research.

3.1 Work at Argonne National Laboratory

Contributors: Y. Miao, B. Ye, Z. Mei, G. Hofman, A. Yacout

3.1.1 Research on uranium silicide

3.1.1.1 Rate Theory Modeling for Steady State Operation

Based on the rate theory model parameters developed for U_3Si_2 at LWR conditions, detailed simulations were performed to examine the fission gas behavior during steady state operations in LWRs. In addition to the previous simulations that assumed a 180 K temperature difference from fuel centerline to surface, the influence of temperature gradient to the fission gas evolution was assessed to expand the understanding of gaseous swelling and gas release in U_3Si_2, as shown in Figure 3.1. It seems that the appearance of Regime III (red) is facilitated by the temperature gradient. This makes sense as temperature gradient helps enhance the Xe diffusion on grain boundaries. In summary, severe intergranular gaseous swelling and consequent gas release only occurs at high temperatures ($>$1000 K) with sufficient temperature gradient.

As predicted by the rate theory simulations, the fission gas behavior in U_3Si_2 is dependent on a series of factors including fuel temperature and temperature gradient, rather than the fission density itself. Thus, it would significantly enhance the credibility of BISON simulations to replace the research reactor data based swelling correlation with the rate theory data based correlation. Thus, it is assumed that the gaseous swelling in U_3Si_2 is only dependent on three variables: temperature (T), temperature gradient (G), and fission density (f). The following empirical function was used to fit the gaseous swelling data produced by the GRASS-SST code:

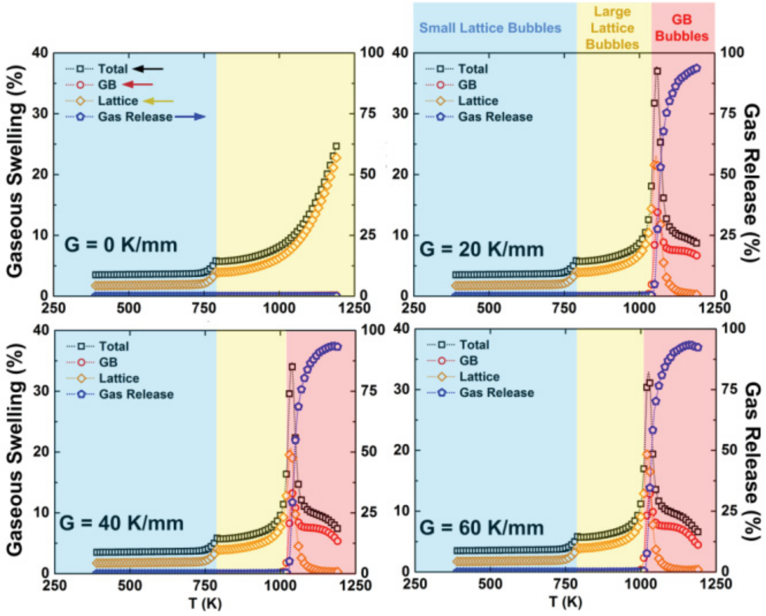

Figure 3.1: Three temperature regimes of fission gas behavior in U_3Si_2.

$$\left(\frac{\Delta V}{V}\right)_{gaseous} = a_1 f^2 + a_2 f + a_3 \left(e^{a_4 f} - 1\right) \tag{3.1}$$

where, a_i's are functions of G and T and were fitted to the rate theory results. This correlation has been embedded into the BISON fuel performance code.

3.1.1.2 Rate Theory Model Development for LOCA Scenarios

In addition to those fission gas parameters involved in the steady state rate theory model, the behavior of overpressurized and underpressurized fission gas bubbles is important to the power transients. In order to simulate the fission gas behavior during LOCA in LWRs, the growth of overpressurized bubbles and the shrinkage of underpressurized bubbles are governed by diffusion creep of the matrix, which is controlled by the diffusion of point defects. The diffusivities of both interstitials and vacancies of U_3Si_2 were calculated using DFT with the same setup as in the Xe diffusivity calculation. The diffusion mechanism of uranium vacancy and interstitial with highest corresponding diffusivities were selected to be the estimates of the parameters controlling the growth and shrinkage during power transients: $D_{o,v}$ = 7.53×10^{-6} m^2/s, Q_v = 2.13 eV, $D_{o,i}$ = 1.05×10^{-5} m^2/s, and Q_i = 1.68 eV. Additionally, in the GRASS-SST rate theory model, the overpressurized bubbles have a different diffusion mechanism that is enhanced by surface diffusion. Due to the lack of experimental and computational data for the surface diffusion in U_3Si_2 , related parameters were adopted from the existing well-developed UO_2 model.

The rate theory simulation of LOCA utilizes input parameters produced by the BISON code. In the BISON-based LOCA simulation, the base simulation was run for approximately 40,000 MWD/tU average burnup prior to the introduction of the 70-second LOCA. During the LOCA, the fuel temperature drops first due to the loss of power, and then increases up to 1000 K due to the absence of coolant. Meanwhile, additional gaseous swelling was found during the LOCA. Analysis on the size distribution of fission gas bubbles before and after LOCA shows that that additional gaseous swelling mainly originates from the growth of overpressurized bubbles due to thermal inflation, although coalescence of small bubbles also occurs (see Figure 3.2). More importantly, fission gas was found to stay in intragranular bubbles even after the LOCA, implying controllable gaseous swelling and suppressed gas release.

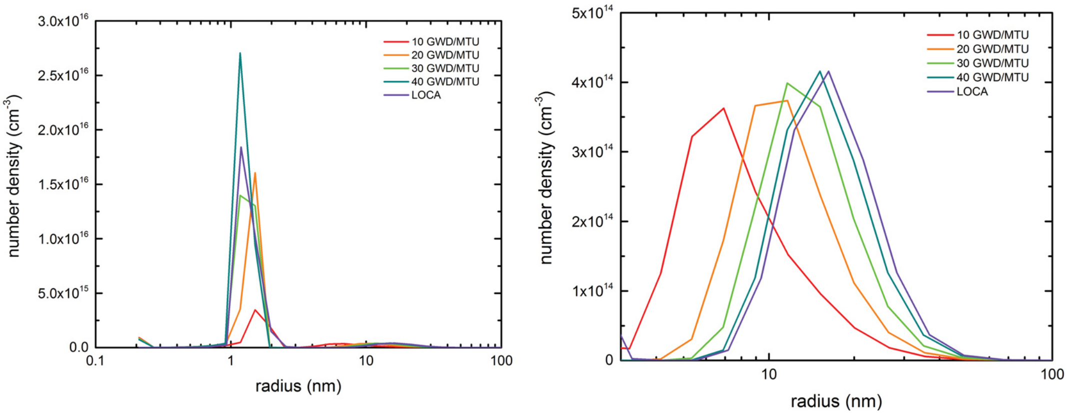

(a) **(b)**

Figure 3.2: Intragranular bubble size distribution throughout the fuel life cycle (a) bubble size distribution from 0.2 nm to 100 nm in radius; (b) bubble size distribution near the large size peak.

3.1.1.3 Ion Irradiation Experiments to Simulate In-Pile Fuel Performance

Ion irradiation was used to simulate the in-pile irradiation condition so as to examine the radiation damage as well as the fission gas bubble morphology in U_3Si_2 in a short term. The ex situ ion irradiation experiment was done at Argonne Tandem Linac Accelerator System (ATLAS) using an 80 MeV high-energy Xe ion beam to replicate the fission product energy. The U_3Si_2 pellets were irradiated to 300 dpa (which corresponds to a peak Xe concentration equivalent to a 5% burnup) at 573 K, 723 K, and 873 K (which cover the typical operation temperature range of U_3Si_2 in LWRs). Further post-irradiation examinations will be performed to provide valuable reference to the improvement of the rate theory models. The in situ ion irradiation experiment was done at IVEM-Tandem facility using a 1 MeV Kr ion beam to investigate the amorphization threshold of U_3Si_2 at different temperatures. No amorphization was observed in U_3Si_2 up to 10 dpa at room temperature or up to 60 dpa at 573 K. Room temperature experiment is not consistent with the 0.3 dpa threshold found in an arc-melt U_3Si_2 sample. As the samples used in this study were sintered, the difference in manufacture techniques may lead to the different amorphization behavior. Further in situ experiments will be conducted to confirm this hypothesis.

3.2 Work at Idaho National Laboratory

Contributors: Y. Zhang, D. Schwen, L. Aagesen, K. Ahmed, J. Yu, B. Beeler, C. Jiang.

To utilize U_3Si_2 and FeCrAl in realistic fuels, the primary challenge is that their in-pile and out-of-pile behaviors have not been extensively tested for fuel safety and reliability. Meanwhile, the current understanding from material science point of view is far from sufficient to develop a theoretical prediction of their performance. To accelerate the understanding and to reduce the cost of experimental studies, multiscale modeling and simulations in analogy to that for UO_2 fuel are utilized to improve the fundamental standing and to develop materials models. Moreover, for U_3Si_2 and FeCrAl, tools required for studies at the atomistic scale and mesoscale are yet to be developed. In FY16, lower-length-scale efforts have been made to develop the needed tools at various scales and to develop engineering scale materials models for certain properties, following a long-term objective of replicating the success on U_3Si_2 fuel achieved under the NEAMS program. In what follows, progress made at the lower-length-scale is summarized. For more details, please refer to a more detailed report [22].

3.2.1 Research on uranium silicide

Two interatomic potentials, one Tersoff type and one modified embedded-atom-method type, have been developed for U_3Si_2 with the focus on phase stability and elasticity. Extensions of the potentials have been made to include Xe for the purpose of simulating fission gas. The potential may also be used to describe other U-Si compounds such as U_3Si. These potentials will be utilized to calculate the interfacial energies, defect formation energies and their interactions with fission gas and interfaces, and to simulate defect production in U_3Si_2 for the purposes of improving fundamental understanding and providing input for upper scale models.

A Kim-Kim-Suzuki (KKS) phase field model has been developed in MARMOT for the phase stability of U-Si compounds including U_3Si_2, USi, U_3Si, and liquid phases. Free energies from the CALPHAD database have been taken and implemented. The model correctly reproduced three-phase coexistence in a U_3Si_2-liquid-USi system at the eutectic temperature, solidification of a three-phase mixture below the eutectic temperature, and complete melting of a three-phase mixture above the eutectic temperature. This model, with some more parameters to be provided from atomistic calculations, will be used to investigate phase evolution during fuel operation and possible fuel melting at accident scenarios.

A phase field model has been developed in MARMOT for gas bubble swelling. A unique feature of this model is that it can describe the formation of voids and bubbles when the global concentration is dilute but well above the thermal equilibrium. Currently, material parameters are being collected to enable gas bubble formation simulations in U_3Si_2. In FY17, this model will be used to estimate gas bubble swelling in U_3Si_2 fuel. Comparison of gas bubble swelling in U_3Si_2 and UO_2 will also be compared.

A thermal conductivity model for unirradiated U-Si compounds has been developed and implemented into BISON. This model describes the thermal conductivity of a certain U-Si compounds as a function of Si content and temperature. It is fitted using experimental data for U, U_3Si_2, U_3Si_5, and Si, and shows good predictivity for U_3Si and USi. In FY17, the model will be extended to include degradation caused in lattice defects and will be used in MARMOT simulations to assess the effect of gas bubbles.

3.2.2 Research on FeCrAl

A lattice kinetic Monte Carlo model has been developed for Fe-Cr and Fe-Al binary alloys by fitting the bond energies using density functional theory calculations. In the fitting, an arbitrary assumption, which depicts the second nearest neighbor interaction to be fractional of that of the first and is widely used for convenience in previous models, is abandoned for better accuracy. In FY17, the model will be improved by including composition-dependent bond energies for Fe-Cr, and extended for Fe-Cr-Al ternary systems. The ternary system will be used to study precipitation in FeCrAl alloys under thermal aging and neutron irradiation.

3.3 Work at Los Alamos National Laboratory

3.3.1 Research on uranium silicide

Contributors: D. A. Andersson, M. J. Noordhoek, S. C. Middleburgh, B. Beeler, M. I. Baskes, Y. Zhang, T. M. Besmann, , R. W. Grimes, E. J. Lahoda, A. Chernatynskiy, C. R. Stanek

Uranium silicides, in particular U_3Si_2, are being explored as an advanced nuclear fuel with increased accident tolerance as well as competitive economics compared to the baseline UO_2 fuel. During FY16 we have worked on several tasks connected to atomistic modeling of the proposed ATF fuels: 1) Development and validation of a robust methodology to study U-Si compounds, including the U_3Si_2 fuel candidate, using density functional theory (DFT) calculations [23], 2)

Extension of this methodology to neighboring actinides in order to assess the behavior of the uranium f electrons and their importance to the structure and properties of U-Si compounds [24], 3) Based on the DFT methodology in 1) the U-Si phase diagram was investigated in the U_3Si_2 region focusing on the possibility of a non-stoichiometric U_3Si_2 phase [25] , 4) Together with INL we worked on the modified embedded atom method (MEAM) empirical potential for the U-Si system, which includes a preliminary Xe potential, 5) Simulation of fission gas bubble resolution in U-Si compounds using the binary collision approximation, 6) We have contributed to work led by INL aimed at modeling the thermal conductivity of U-Si compounds and 6) The DFT methodology referenced in 1) was applied to study defect and fission gas properties in U_3Si_2. In this summary we are only going to touch on a few highlights and we will not cover all of these topics.

DFT calculations were used with spin-orbit (SO) coupling and on-site Coulomb correction (GGA+U) methods to investigate the U-Si system [23]. Structure prediction methods were employed to identify alternate stable structures to those identified in experiments. Convex hulls of the U-Si system were constructed for each of the methods to highlight the competing energetics of various phases (Figure 3.3). For GGA calculations, new structures are predicted to be dynamically stable, but these have not been experimentally observed. When the GGA+U (Ueff $>$ 1.3 eV) method is considered, the experimentally observed structures are predicted to be energetically preferred. Phonon calculations were used to investigate the energy predictions and showed that the use of the GGA+U method removes the imaginary frequencies observed for U_3Si_2 when the correction is not considered. Total and partial electron density of states calculations were also performed to understand the role of GGA+U methods and orbitals on the bonding of U-Si compounds.

Applying the DFT methodology assessed in Ref. [23] and thermochemical analysis, the stability of U_3Si_2 with respect to non-stoichiometry reactions in both the hypo- and hyper-stoichiometric regimes was assessed (Figure 3.4). We found that the degree of non-stoichiometry in U_3Si_2 is much smaller than in UO_2 and at most reaches a few percent at high temperature. Non-stoichiometry impacts fuel performance by determining whether the loss of uranium due to fission leads to a non-stoichiometric $U_3Si_{2\pm x}$ phase or precipitation of a second U-Si phase. We have also investigated the U_5Si_4 phase as a candidate for the equilibrium phase diagram.

3.3.2 Research on FeCrAl

Contributors: A. Patra, W. Wen, E. Martinez, L. Capolungo, C. N. Tomé

FeCrAl cladding behavior is being studied with crystal plasticity at Los Alamos National Laboratory. The focus of the work during the year has been: 1) development of crystallography-based polycrystal models to describe plastic deformation of irradiated FeCr alloys; 2) implementation of such model in MOOSE; 3) development of a polycrystal model for thermal creep of FeCr alloys; 4) first principle derivation of interaction strength between dislocation and loops.

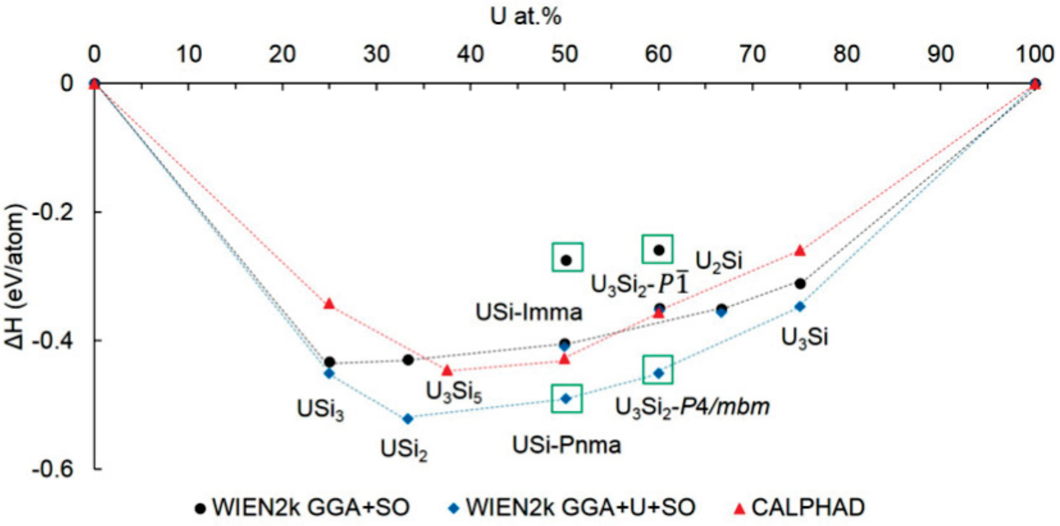

Figure 3.3: The convex hull for U-Si compounds using GGA+SO and GGA+U+SO calculations. Black circles and corresponding dashed lines are the GGA+SO values. Blue diamonds and corresponding dashed blue line are GGA+U+SO calculations with Ueff = 1.5 eV. The green boxes are guides for the eye that highlight USi-Pnma and U_3Si_2-P4/mbm values (Pnma and P4-mbm designate the space group). U_3Si_2-P4/mbm and USi-Pnma are the experimentally proposed crystal structures, which are reproduced by the GGA+U+SO but not the GGA+SO calculations. Red triangles and the corresponding dashed line represent the convex hull from CALPHAD. The GGA+U+SO values can be brought close to the experimental values by applying an alignment scheme required to compare regular GGA (uranium metal) and GGA+U (uranium silicides) values (not shown).

3.3.2.1 Modeling the irradiation hardening behavior of FeCrAl alloys using crystal plasticity simulations

A defect based constitutive crystal plasticity model was implemented in the Visco Plastic Self Consistent (VPSC) framework to simulate the mechanical response of FeCrAl alloys post-irradiation. Irradiation induced <111> and <100> dislocation loops, and precipitates are used as state variables in this framework. The model parameters were calibrated to tensile loading experiments performed at ORNL by K.G. Field et al. on unirradiated Fe-15Cr-4Al alloy. Texture induces anisotropic response and was accounted for. Figure 3.5(a) shows the comparison of model predictions with the experimental stress-strain data at room temperature. The model was then used to predict the irradiation hardening behavior for alloys with varying compositions. Figure 3.5(b) shows the comparison of model predictions of the initial yield stress with experiments for alloys irradiated to 1.6 dpa damage. The model reproduces the observed increase in yield stress due to irradiation hardening with reasonable confidence. Moreover, the subsequent hardening behavior (not shown here) is consistent with experiments, where the stress-strain re-

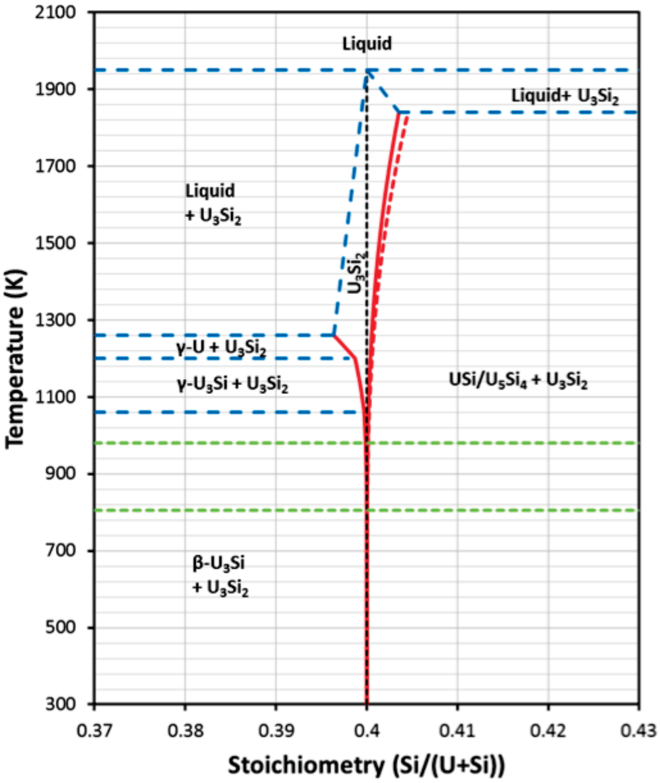

Figure 3.4: Predicted phase field for U_3Si_2 from mass action analysis of the defect concentrations. The red lines show the extent of deviation in stoichiometry of U_3Si_2 (the dashed red line considering USi instead of U_5Si_4 as the Si-rich reference phase). Dashed blue lines indicate portions of the phase diagram not calculated in this work. Green lines show typical center-line and outer pellet temperatures for the U_3Si_2 pellet.

sponse is essentially flat following initial yield.

3.3.2.2 Demonstration of finite element simulations in MOOSE using crystallographic models of irradiation hardening and plastic deformation

The crystal plasticity constitutive framework for irradiation hardening and plastic deformation described above was interfaced with the FE code MOOSE as a material routine. This accomplishment will allow us to utilize mechanism-based laws in simulations of complex non-homogeneous reactor conditions (such as LOCA). As an example, we demonstrate this interface for an application consisting of straining in tension a 3D bar of Fe-15Cr-4Al. The tensile specimen was assumed to have experienced a non-homogeneous radiation dose that varies from 1.6 dpa at the bottom to 0.0 dpa at the top. Simulation shows that regions with higher dpa are less

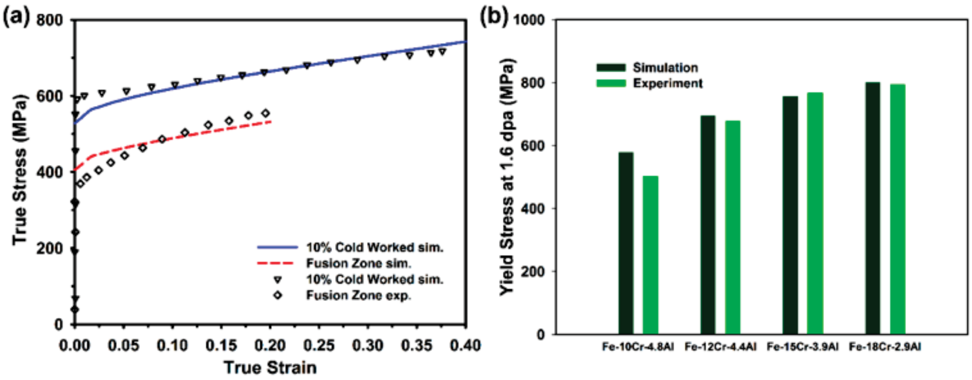

Figure 3.5: (a): Model predictions of the stress-strain response of cold worked and fusion zone specimens of Fe-15Cr-4Al laser weld alloys compared with experiments; (b): Comparison of the predicted yield stress with ORNL experiments for various FeCrAl alloys irradiated to 1.6 dpa damage.

compliant and deformation tends to localize in regions with low dpa (1.6% vs 11.8% strain, see Figure 3.6).

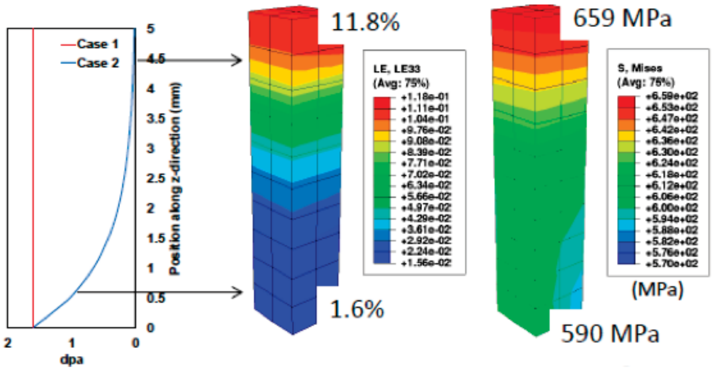

Figure 3.6: VPSC-MOOSE prediction of local stress and strain in Fe-15Cr-4Al deformed in tension to 5% total strain. Dose profile (left); plastic strain distribution (center); stress distribution (right).

3.3.2.3 A physics-based crystallographic modeling framework for describing the thermal creep behavior of Fe-Cr alloys

A constitutive model was implemented in VPSC, based on the evolution of dislocations gliding on (111) and (112) planes, overcoming MX precipitates randomly dispersed and other dislocations, and getting stored in cell walls inside the grain. The model depends explicitly on several physical features, such as climb mechanisms, diffusivity of vacancies, dislocation recombination, intra-granular stress distributions, and activation energies. The model captures the creep results reported by Basirat et al. (University of Idaho) for Fe-9Cr-1Mo steel tested through a variety of temperature and stress conditions, which exhibit orders of magnitude in creep rates. An example of predicted results is shown in Figure 3.7.

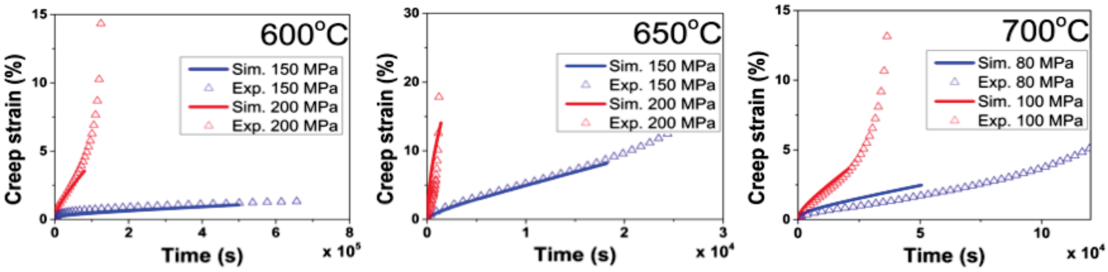

Figure 3.7: Predicted creep strain for Fe-9Cr-1Mo steel at several temperatures and tensile stresses. Comparison with experimental data from [Basirat et al, Int. J. Plast. 37 (2012) 95].

3.3.2.4 Thermal activation of dislocation-obstacle bypass

The interaction between dislocations and irradiation produced defects plays a central role in the hardening and creep models described above. A basic understanding of such interactions provides a stronger physical basis to predictive models. During FY16 we have developed a novel Discrete Dislocation Dynamics (DDD) methodology that couples traditional approaches with the nudged-elastic band (NEB) method. The main goal is to be able to compute the minimum energy path between obstacles in a computationally efficient way that will result in statistically representative values. As a first application relevant to the project, we have studied the interaction of an edge dislocation with <100> self-interstitial clusters (Figure 3.8). Moreover, we have also calculated the vibrational frequencies of the dislocations at the equilibrium and at the saddle points, that relying on a harmonic transition state theory description of the process gives us access to the rate for the dislocation to overcome the obstacle: $\Gamma_{TST} = \nu \cdot \exp((-\Delta E)/kT)$. The inverse of this rate is the waiting time that the dislocation has to spend on average before a thermal fluctuation takes it to the other side of the obstacle, which is the waiting time needed in crystal plasticity calculations.

This development has led to three manuscripts, where the methodology is described in detail. These manuscripts are currently under review, two in the Journal of Mechanics and Physics of Solids and the third one in Acta Materialia.

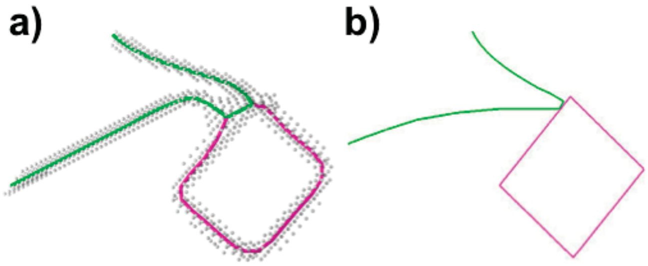

Figure 3.8: Predicted creep strain atomistic (a) and continuum (b) details of the dislocation-100 self-interstitial loop interaction.

3.4 Work at University of Tennessee, Knoxville

Contributors: S. Blondel, D. Dasgupta, A. Kohnert, B. Wirth

In order to improve the accident tolerance of light water reactor (LWR) fuel, alternative cladding materials have been proposed to replace zirconium (Zr)-based alloys. Of these materials, there is a particular focus on iron-chromium-aluminum (FeCrAl) alloys due to much slower oxidation kinetics in high-temperature steam than Zr-alloys. This should decrease the energy release due to oxidation and allow the cladding to remain integral longer in the presence of high temperature steam, making accident mitigation more likely. As a continuation of the development for these alloys, the material response must be demonstrated to provide suitable radiation stability, in order to ensure that there will not be significant dimensional changes (e.g., swelling), as well as quantifying the radiation hardening and radiation creep behavior.

Information is needed to determine the suitability of these iron-chrome-aluminum alloys as fuel cladding and assess safety margins for their operation. In particular, these Fe-Cr-Al alloys will experience neutron irradiation and potential radiation effects on the dimensional stability and mechanical properties. In particular, the cladding material response must be demonstrated to provide suitable radiation stability, as well as quantifying the radiation hardening and radiation creep behavior. In this report, we describe the extension of a discrete cluster dynamics model to incorporate a grouping scheme to enable the prediction of high dose defect cluster evolution, as well as provide a preliminary assessment of the neutron radiation response of FeCrAl with respect to the defect physics and damage accumulation behavior.

Cluster dynamics methods are a powerful rate theory approach developed to simulate and analyze the kinetics of evolving material microstructures. These models are particularly useful in studying radiation damage, where they have been applied to processes as varied as noble gas behavior and bubble formation [26–28], dislocation loop nucleation [29–32], and radiation induced and enhanced precipitation [33, 34] with potential applications to radiation creep and solute segregation. These methods rely on evolving a set of coupled – and often spatially dependent – differential equations through time.

Each equation represents the concentration of a particular defect or solute species and takes the form

$$\frac{\partial C_i}{\partial t} = D_i \nabla^2 C_i - D_i k_i^2 C_i + R_i(\boldsymbol{C}) + g_i \tag{3.2}$$

where C_i is the concentration of the ith species, D_i is its diffusivity, k_i^2 is the net sink strength for its removal, g_i is its source rate, and $R_i(\boldsymbol{C})$ is the rate of consumption or production through interaction with other species. The equations are coupled through these reaction rates. As an example, one might construct a problem where each C_i represents the population of precipitates containing i atoms and the reaction terms describe the depletion of smaller clusters and appearance of larger ones as solutes arrive at the existing precipitate distribution.

These methods demonstrate a substantial improvement over the “classical rate theory” approach in that they compute the full size distribution of irradiation induced damage features rather than a single average population. A major advantage of this approach is that the nucleation phase of damage formation can be treated consistently with growth, where older methods must assume feature densities or alternative nucleation models [35–37]. These methods, however, must overcome a significant technical hurdle for broad application. As posed, the natural resolution for cluster dynamics is of the atomic scale, but the desired scale to model engineering relevant microstructural changes involves defects or features with sizes of nanometers to hundreds of nanometers. As an example, it requires on the order of 10^8 equations to simulate the formation of voids a few tens of nanometers in diameter. This may prove manageable given a limited number of reaction pathways, but if the number of constituents increases, as for modeling gas bubbles or complex precipitates, the situation becomes completely infeasible.

This combinatorial explosion has typically limited the application of cluster dynamics to the description of small, simple systems, and for larger or more complex systems researchers have turned to other methods. Kinetic Monte Carlo (KMC) [38, 39] and stochastic cluster dynamics (SCD) [40–42] methods have offered an attractive alternative to the deterministic approach. These methods do not suffer from the combinatorial explosion from large or multi-component cluster spaces in the same way that deterministic approaches often do. These methods offer a number of additional potential advantages as well. For instance, object KMC models do not require the rate constants embedded in cluster dynamics which are computed from mean field conditions and may be incorrect under certain circumstances such as during spatially correlated damage events. While moving to stochastic approaches makes a solution feasible, the cost associated with attaining damage doses relevant to major microstructural changes is quite high and most such simulations reach terminal doses of a few displacements per atom (dpa) or less. These methods have not yet demonstrated the capability to model the microstructural changes in fuels or in structural materials for fast reactors, which must endure doses of hundreds of dpa or more.

While not discussed in any detail here, we have focused our effort during the past year to evaluating a number of different grouping schemes to extend the applicability of cluster dynamics models that solve a system of equations such as given in Eq. 3.2. We find that the most general and reliable method involves the use of a moment approach to grouping the equations, although several different interpolation schemes show promise. We have a revised journal article under review that describes this analysis, and more information will be forthcoming once the article is accepted.

We have begun to use the moment-based grouping method of cluster dynamics to evaluate the radiation damage microstructure development in an Fe-Cr-Al alloy subject to neutron irradiation at a dose rate of 8.1×10^{-7} dpa/s as a function of irradiation temperature between 320 and 400°C to radiation doses of 1.6 and 2.4 dpa. Figure 3.9 shows the initial modeling results for the mean size (top) and density (bottom) of self-interstitial type dislocation loops as a function of Burgers vector, namely a<100> (left) or a/2<111> (right), as a function of irradiation temperature. The initial modeling results shown in Figure 3.9 correctly reproduce the observed experimental result that the <100> loops are larger than the <111> loops, but neither the size nor magnitude is correctly predicted at this time.

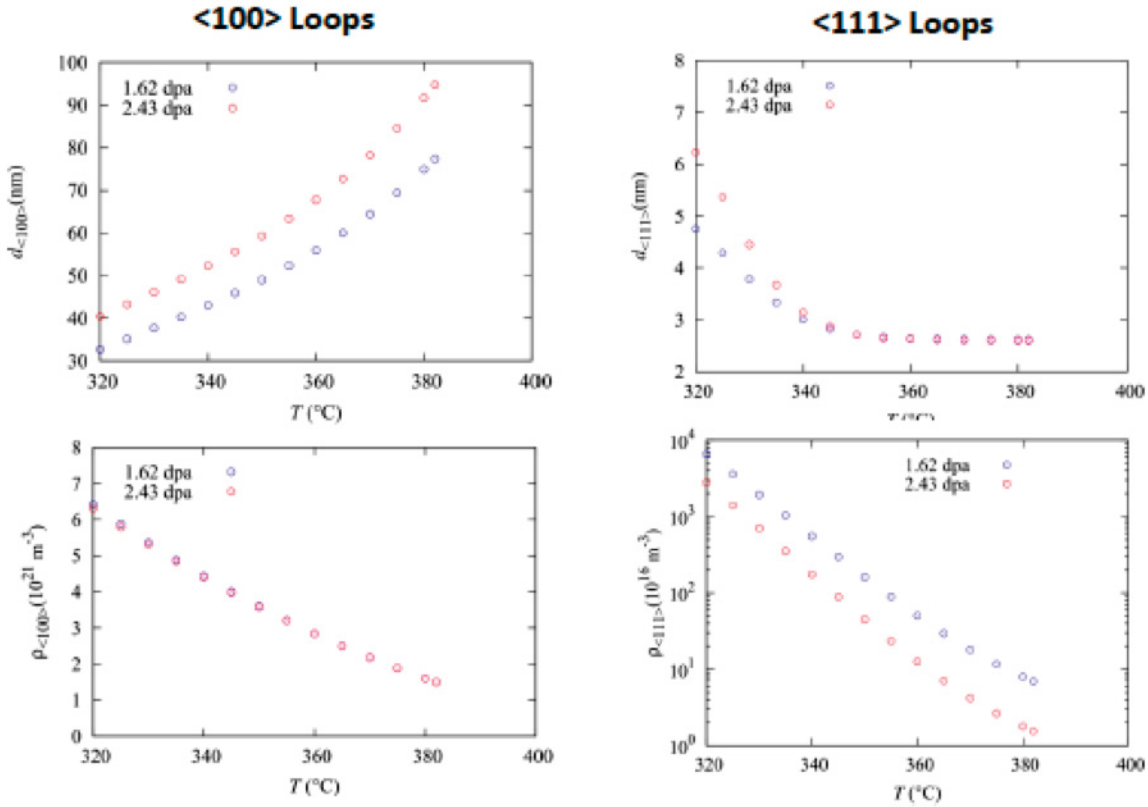

Figure 3.9: Cluster dynamics modeling predictions of dislocation loop mean size (top) and number density (bottom), for loops with Burgers vector of a<100> (left) and a/2<111> (right), as a function of irradiation temperature and dose (1.6 dpa is blue and 2.4 dpa is red circles).

Future efforts will continue to evaluate the assumptions about the thermodynamic and kinetic properties of the defect clusters in FeCrAl, as well as broadening the comparison of model predictions to other experimental results, and calculating the net flux of defects to dislocations that can provide the driving force for dislocation climb under irradiation, leading to irradiation creep. These initial results provide promise that the cluster dynamics modeling can successfully predict the radiation damage of microstructures in nuclear fuel cladding and aid in the development of advanced constitutive models needed in fuel performance modeling.

4 Engineering Scale Developments

At the engineering scale exploratory studies have been completed to investigate the behavior of the two ATF concepts under normal operating and accident conditions. In this section, the material models incorporated into BISON for FeCrAl and U_3Si_2 are summarized. Examples are provided that compare the response of the ATF concepts to that of traditional fuel rods containing UO_2 fuel and Zircaloy cladding under various operating conditions. Finally, sensitivity analyses are completed to determine the most important material parameters on output metrics of interest including fuel centerline temperature and cladding hoop strain.

4.1 Material Models

While the lower length scale models are being developed, empirical correlations have been implemented into BISON. The materials of interest include U_3Si_2 fuel and the FeCrAl alloy being developed at Oak Ridge National Laboratory (ORNL) known as C35M [43].

4.1.1 U_3Si_2 Fuel

Uranium silicide is of particular interest because of its considerably higher thermal conductivity compared to UO_2, which will result in lower fuel temperatures and temperature gradients within the fuel. Lower thermal gradients are expected to result in less cracking of the fuel pellets. Less cracking and lower temperatures suggests that fission gas release will be less in U_3Si_2 than in UO_2. Moreover, U_3Si_2 has a higher uranium density than oxide fuel resulting in economic savings, as fuel enrichment is not necessary to achieve the same discharge burnup. Unfortunately the majority of existing experimental data for U_3Si_2 is for low temperature dispersion fuel used in research reactors. The applicability of the models developed using this data to U_3Si_2 in pellet form under LWR conditions is unclear.

4.1.1.1 Mechanical properties

Since no thermal and irradiation creep data exists for U_3Si_2, the fuel is treated as an elastic material with a Young's modulus of 140 GPa and a Poisson's ratio of 0.17 [12].

4.1.1.2 Thermophysical properties

Using the existing data, empirical correlations have been added to BISON for thermal conductivity and specific heat. The thermal conductivity and specific heat used in the work presented in this report was proposed by White et al. [6].

The thermal conductivity correlation in W/m-K is:

$$k = 0.0151T + 6.004 \tag{4.1}$$

where T is the temperature in K. A comparison of the unirradiated thermal conductivity of U_3Si_2 and UO_2 as a function of temperature is shown in Figure 4.1. Only the unirradiated thermal conductivities are compared because the change of thermal conductivity of U_3Si_2 under irradiation is currently not known. The UO_2 curve is that which is obtained from the NFIR thermal conductivity model with burnup and gadolinia content set to zero. The figure indicates that for fresh fuel the thermal conductivity of U_3Si_2 is much larger than that of UO_2. The curves are terminated at a temperature of 1773 K because White's U_3Si_2 model is only valid up to that temperature.

Recently, a new thermal conductivity model has been added to BISON based upon the lower length scale work of Yongfeng Zhang at the Idaho National Laboratory. This model was developed using phase field calculations and improves upon White et al.'s model by predicting the thermal conductivity of a variety of the secondary uranium silicide phases including U_3Si and U_3Si_5. The Zhang model reproduces the behavior of the White et al. correlation for U_3Si_2.

The correlation for specific heat in J/mol-K is:

$$C_p = 0.02582T + 140.5 \tag{4.2}$$

To obtain the specific heat in units of J/kg-K, one must divide the specific heat calculated by Eq. 4.2 by the molar mass for U_3Si_2 given as 0.77026 kg/mol.

The thermal expansion coefficient is set to 15×10^{-6} K^{-1} according to Metzger et al. [12].

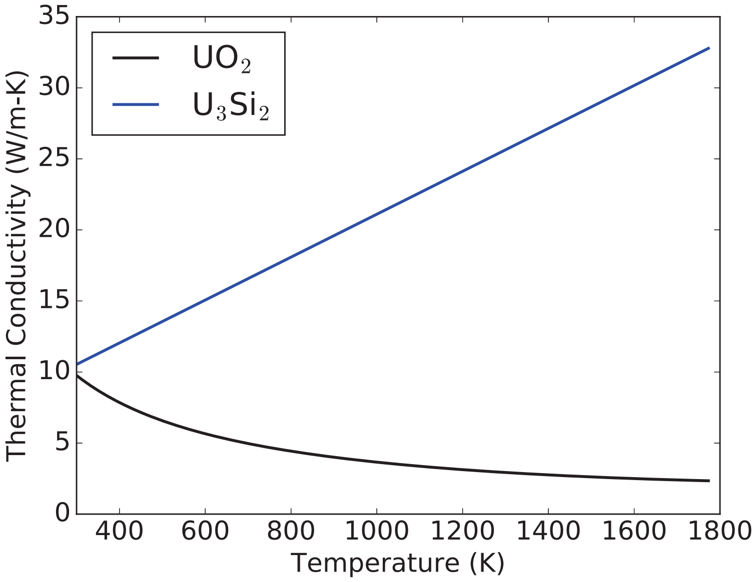

Figure 4.1: Comparison of the unirradiated thermal conductivity of U_3Si_2 and UO_2 as a function of temperature.

4.1.1.3 Swelling and densification

The default swelling and densification model in BISON was originally derived by Metzger et al. [12] from experimental data from Finlay et al. [11]. Metzger et al. converted the data in Figure 3 of Finlay et al. into swelling strain as a function of burnup (in FIMA) by utilizing a conversion factor from fission density (in fissions per cubic centimeter) to FIMA of 3.63457×10^{-23}. The obtained empirical correlation is given by

$$\frac{\Delta V}{V_o} = 3.88008 Bu^2 + 0.79811 Bu \tag{4.3}$$

The above correlation represents the total swelling strain due to both gaseous and solid fission products. This model was separated into its gaseous and solid components in preparation for a new gaseous swelling model based upon rate theory by Yinbin Miao at Argonne National Laboratory. The Miao gaseous swelling model is more sophisticated because it takes into account the effect of local power, local temperature and temperature gradient within the fuel pellet. The Miao model has been developed for both normal operating and transient conditions. The general form of the Miao formula is given by Equation 3.1. The solid swelling based upon Finlay's data is given by:

$$\left(\frac{\Delta V}{V_o}\right)_{solid} = 0.34392 Bu \tag{4.4}$$

and the gaseous swelling based upon Finlay's data is given by:

$$\left(\frac{\Delta V}{V_o}\right)_{gaseous} = 3.88008Bu^2 + 0.45419Bu \tag{4.5}$$

4.1.1.4 Fission gas behavior

Compared to UO_2, fuel temperatures will be much lower in U_3Si_2 due to a higher thermal conductivity, which would tend to mitigate fuel gaseous swelling and fission gas release. However, recent lower-length scale work [44] indicated that the fission gas diffusion coefficient is much higher, at a given temperature, for U_3Si_2 than for UO_2. Indeed, an experiment performed on U_3Si_2 at power reactor temperatures [45] demonstrated that significant fission gas release and gaseous swelling occur, even at very low burnup. Hence the need to develop suitable fission gas behavior models in order to properly analyze the performance of fuel systems with $U_3Si_2$is clear. To do so, there is a need for both theoretical model development and generation of experimental data to support model validation.

Recently, work was performed along these directions at INL. In particular, (i) new experimental data of the gaseous swelling in U_3Si_2 under power reactor conditions was generated from [45], and (ii) the development of a new theory-based model for the analysis of fission gas behavior of U_3Si_2 in BISON was started.

The first item aims to partly fulfill the need for data for validation of any newly developed engineering scale model. The second item aims to allow for fission gas behavior calculations on the engineering scale informed by lower length scale modeling for the determination of the fundamental model parameters. Moreover, theory-based modeling overcomes the limitations related to the use of purely burnup dependent correlations for gaseous swelling (Section 4.1.1.3), such as the impossibility of predicting fission gas behavior during rapid transients, or difficulties in extending the validity range of correlations to power reactor conditions.

More details of this recent work are given in the following subsections.

Generation of new experimental data
Several U_3Si_2 irradiation experiments have been conducted in research reactors, e.g. [46–48], and experimental data of gas bubble evolution and gaseous swelling at research reactor fuel temperatures ($\sim$300-500 K) are available. However, fission gas behavior at power reactor temperatures is expected to be significantly different, and affected by the different structure of the fuel (which is crystalline at power reactor temperatures [45] as opposed to amorphous at low temperature).

It follows that the development of a U_3Si_2 fission gas behavior model for power reactor temperatures cannot rely only on experimental data made available so far [49]. To the best of our

Table 4.1: Pre- and post-irradiation grain-size measurements for the fuel slug from the AI-7-1 irradiation experiment of a U_3Si_2 fuel rod.

	Linear intercept (μm)	3D grain radius (μm)
Fresh fuel	61±15	46±12
Fresh fuel	35±9	26±7
Irradiated fuel	37±9	28±7

knowledge, only one experiment on U_3Si_2 fuel irradiated in power reactor conditions has been performed [45]. This experiment is referred to as AI-7-1, performed by Atomics International in 1960 to determine U_3Si_2 irradiation behavior characteristics, i.e., dimensional stability and fission gas release. Several metallographic images were produced during the AI-7-1 experimental campaign, but no direct measure of the gaseous swelling and of the grain size had been performed.

In the present work, we measured the gaseous swelling and the grain size of a U_3Si_2 fuel sample irradiated at power reactor temperature, based on a post-irradiation metallographic image from [45]. The U_3Si_2 fuel sample was irradiated at 46 kW/m up to 7.3 GWd/tU. The sample experienced an estimated temperature of 950 K and a local burnup of 6.0 GWd/tU.

Then, the present work led to the first U_3Si_2 gaseous swelling data at power reactor temperatures. Thus, even if limited in number, the data generated in this work are of fundamental importance for the development and validation of any engineering scale fission gas behavior model for U_3Si_2.

The metallography used for generating the new data is reported in Fig. 4.2. We used the image analysis software Image J [50] and adopted the measuring methodology described in [51].

The measured volumetric gaseous swelling is 12%. We also singled out the contributions from intra- and inter-granular bubbles, resulting in swelling values of 2.8% and 9.2%, respectively. The relative uncertainty of these measurements is estimated as 30%. These results are in agreement with the measured density changes reported in the original report from Atomics International [45].

We measured the grain size from the same metallography used for the swelling measurement (applying methodology from [52]), obtaining an average grain radius of 28±7 μm. Comparing to metallographic images of the same sample before irradiation, there is no evidence of significant grain growth occurring during this experiment (Table 4.1).

Development of a new fission gas behavior model

Since the available experimental evidence at power reactor temperatures is not sufficient to support the development of empirical U_3Si_2 fission gas models, we tackle the development of a

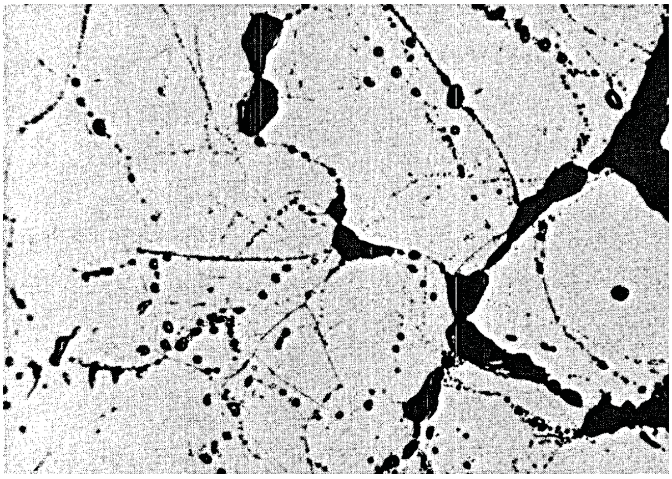

Figure 4.2: Post-irradiation metallographic image (magnification 250x) of the U_3Si_2 fuel slug from the AI-7-1 irradiation experiment considered in this work [45]. Intra- and inter-granular bubbles are clearly observable. The measured intra- and inter-granular gaseous swelling values are 2.8% and 9.2%, respectively . The uncertainty is estimated to be about 30%.

theory-based, multiscale model that relies on the concepts of cluster dynamics as well as lower length-scale calculations for the determination of the basic parameters.

The evolution of intra-granular bubbles in nuclear fuel is controlled by three processes: nucleation, re-solution, and trapping. Considering that fission gas behavior in uranium silicide is characterized by homogenous nucleation and re-solution [53], we write the master equations of cluster dynamics for the homogenous processes. Defining c_n as the concentration of atom clusters (or bubbles) containing n atoms (with c_1 indicating the concentration of single gas atoms), the classic cluster dynamics formulation of the master equations is [54]

$$\begin{aligned} \tfrac{\mathrm{d}c_1}{\mathrm{d}t} &= G - 2\nu + \alpha_2 c_2 - \sum_{n=2}^{\infty} \beta_n c_n + \sum_{n=2}^{\infty} \alpha_n c_n \\ \tfrac{\mathrm{d}c_2}{\mathrm{d}t} &= \nu - (\beta_2 + \alpha_2) c_2 + \alpha_3 c_3 \\ \tfrac{\mathrm{d}c_n}{\mathrm{d}t} &= \beta_{n-1} c_{n-1} - (\beta_n + \alpha_n) c_n + \alpha_{n+1} c_{n+1} \end{aligned} \tag{4.6}$$

where β_n is the probability that a single atom is trapped by a cluster containing n atoms, α_n is the probability that an atom is re-solved from a cluster containing n atoms, and G is the production rate of gas atoms.

The values for the coefficients β_n and α_n, and ν are derived from atomistic and molecular dynamics calculations from [44, 53] in a multi-scale modeling approach.

Since the solution of the full system of (thousands of) master equations is impractical for engineering-scale applications (such as BISON), a simplified approach is developed. Clement and Wood [55] simplified the problem by considering only the moments of the size distribution of the clusters. Assuming that bubbles include all clusters containing two or more gas atoms, we define the total concentration of bubbles N and the mean of the size distribution $\bar{n}$, respectively

$$N = \sum_{n=2}^{\infty} c_n \tag{4.7}$$

$$\bar{n} = \sum_{n=2}^{\infty} n c_n / N \tag{4.8}$$

Combining Eqs. 4.6-4.8, it is straightforward to derive equations for the time derivative of N and $\bar{n}$. After algebraic summation, a first order Taylor expansion in the phase space (i.e., exploiting $(\beta_n, \alpha_n, c_n) = (\beta, \alpha, c)(n) \approx (\beta_{\bar{n}}, \alpha_{\bar{n}}, c_{\bar{n}}) + ...$) combined with the assumption that the nucleation process occurs on a faster time scale compared to the growth process ($\mathrm{d}N/\mathrm{d}t \approx 0$ in the equation for $\mathrm{d}\bar{n}/\mathrm{d}t$) leads to

$$\begin{aligned} \tfrac{\mathrm{d}N}{\mathrm{d}t} &= \nu - \alpha_2 c_2 = \nu - \alpha_2 \phi N \\ \tfrac{\mathrm{d}\bar{n}}{\mathrm{d}t} &= \beta_{\bar{n}} - \alpha_{\bar{n}} \end{aligned} \tag{4.9}$$

The factor $\phi = c_2/N < 1$ is estimated as

$$\phi = \frac{1}{\bar{n} - 1} \tag{4.10}$$

reducing the re-solution rate of dimers α_2 when applied to clusters of size $\bar{n}$.

The implementation of the model described by Eqs. 4.9 in BISON is ongoing. Once completed, the new fission gas model in BISON will be used for the calculation of both fission gas release and gaseous swelling in U_3Si_2 under power reactor conditions. Model validation will be performed based on the available experimental data, including in particular those obtained during the present work and presented above.

4.1.1.5 Neutronic properties

Recently, neutronics calculations have been completed to generate one group averaged cross-sections for U_3Si_2 to be included in the radial power factor burnup model in BISON. Due to the higher uranium density more plutonium is expected to be produced in the rim region of the pellet resulting in a more significant radial profile of the power to the fuel. Table 4.2 presents the one energy group pin averaged cross-sections for U_3Si_2. These cross-sections were calculated using a depletion calculation with DRAGON5.

Table 4.2: One energy group averaged cross sections for U_3Si_2 (in barns).

	^{235}U	^{238}U	^{239}Pu	^{240}Pu	^{241}Pu	^{242}Pu
Fission	23.9101	0.1060	56.8242	0.5939	60.2543	0.4651
Capture	6.4194	0.7540	32.1773	80.0460	21.6194	26.7065
Thermal absorption	30.3248	0.8539	89.0001	80.6386	81.8657	27.1692

A comparison between the UO_2 and U_3Si_2 radial power profiles are shown in Figure 4.3 for a simple regression test consisting of 100 linear finite elements in the radial direction. As expected, the radial profile in U_3Si_2 has more self-shielding due to the higher uranium density. It should be noted that the coefficients in the radial power profile equations are still fitted to UO_2 data and only the cross-sections in the equations have been modified for U_3Si_2 until further data is available.

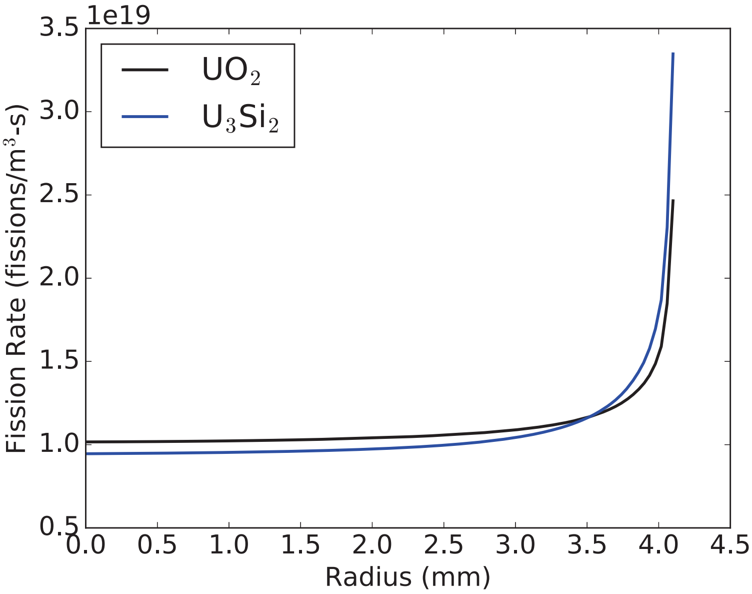

Figure 4.3: Comparison of UO_2 and U_3Si_2 radial power profiles.

4.1.2 FeCrAl Cladding

FeCrAl alloys are widely used in applications where low oxidation rates and high temperature performance are required (e.g., coatings on gas turbines blades). Compared to traditional zirconium based claddings, FeCrAl alloys have higher strength and oxidation resistance, but a lower melting point and higher neutron absorption cross-section. Therefore, thinner cladding walls and slightly larger pellets with higher enrichment will be necessary to compensate for this neutronic penalty. Models have been added to BISON for the C35M alloy being developed at ORNL. When experimental data does not exist, material properties of the commercial alloy Kanthal APMT [56] is used. Models have been added to BISON for temperature dependent Young's modulus, Poisson's ratio, thermal conductivity, thermal expansion and specific heat, thermal and irradiation creep, plasticity, oxidation, and failure. Sweet et al. [57] and Galloway and Unal [58] have performed investigations of Kanthal APMT cladding using BISON. Neither group of authors have committed their material models to the main BISON repository.

4.1.2.1 Mechanical properties

Correlations for Young's modulus and Poisson's ratio have been implemented in BISON from Thompson et al. [59]. The Young's modulus is given by

$$E = -5.46 \times 10^{-5}(T - 273.15)^2 - 3.85 \times 10^{-2}(T - 273.15) + 1.99 \times 10^2 \tag{4.11}$$

while the Poisson's ratio is calculated as follows

$$\nu = 3.85^{-5}(T - 273.15) + 2.68 \times 10^{-1} \tag{4.12}$$

where E (GPa) is the Young's modulus, ν (/) is Poisson's ratio, and T (K) is the temperature.

4.1.2.2 Thermophysical properties

For thermal expansion, thermal conductivity, and specific heat the properties for Kanthal APMT [56] are used, since no data for C35M are yet available. The values for the above mentioned parameters are reported in Table 4.3.

4.1.2.3 Thermal and irradiation creep

Recently, new experimental data on thermal and irradiation creep of C35M FeCrAl alloys have been published by Terrani et al. [60]. Correlations specific to those alloys and accounting for these most recent data have been implemented in BISON. These are described hereinafter.

Thermal Creep

Table 4.3: Temperature dependent thermal conductivity, specific heat, and coefficient of thermal expansion of Kanthal APMT alloy.

Temperature [K]	**Thermal Conductivity [W/m-K]**	**Specific Heat [J/kg-K]**	**Temperature Range [°C]**	**CTE [μm/m-K]**
293.15		480	20 - 250	10.7
323.15	11		20 - 500	12.0
473.15		560	20 - 750	12.2
673.15		640	20 - 1000	12.5
873.15	21	710	20 - 1200	15.1
1073.15	23	670		
1273.15	27	690		
1473.15	29	700		

Thermal creep is modelled through a correlation in the form of a Norton power creep law. Below 873 K, as proposed in [60], the following correlation for thermal creep rate is adopted

$$\dot{\varepsilon} = 2.89 \times 10^{-36} \sigma^{5.5} \exp\left(-\frac{29709}{T}\right) \tag{4.13}$$

while above 873 K the correlation from Saunders et al. [61] is employed

$$\dot{\varepsilon} = 5.96 \times 10^{-27} \sigma^{5.5} \exp\left(-\frac{47136}{T}\right) \tag{4.14}$$

where $\dot{\varepsilon}$ is the creep rate (s^{-1}), σ the effective stress (Pa) and T(K) is the temperature.

Irradiation Creep

Following [60], irradiation creep for C35M alloys is modelled as dependent on the fast neutron flux and on the effective stress. The recommendation in [60] for the irradiation creep rate (s^{-1}) is 5×10^{-6} MPa^{-1} dpa^{-1}. Adopting a conversion factor from dpa to fast neutron fluence of 1×10^{25} n m^{-2} = 0.9 dpa, the following correlation for the irradiation creep rate is obtained:

$$\dot{\varepsilon} = 4.5 \times 10^{-31} \sigma \phi \tag{4.15}$$

where $\dot{\varepsilon}$ is the creep rate (s^{-1}), σ the effective stress (MPa) and ϕ (n m^{-2}s^{-1}) is the fast neutron flux. Eq. 4.15 is implemented in BISON for the calculation of irradiation creep in C35M FeCrAl alloys.

4.1.2.4 Plasticity

An isotropic plasticity model for the C35M FeCrAl alloy has been implemented in BISON. The model calculates the yield stress as a function of temperature based upon data by Yamamoto et al. [62], reported in Table 4.4. This model enables accounting for treatment of plastic deformation in FeCrAl claddings with BISON.

Table 4.4: Yield Stress as a Function of Temperature

Temp. Range [K]	Yield Stress [MPa]
290.735	446.819
546.411	313.964
640.150	295.872
824.832	225.901
1007.24	67.237

4.1.2.5 FeCrAl Failure

A failure model for FeCrAl cladding has been implemented in BISON, based upon an overstress criterion. In facts, when the hoop stress exceeds the ultimate tensile strength (UTS), the cladding is considered failed. The ultimate tensile strength is calculated as a function of temperature based upon experimental data by Yamamoto et al. [62], reported in Table 4.5.

Table 4.5: Ultimate Tensile Strength as a Function of Temperature

Temp. Range [K]	UTS [MPa]
294.738	569.475
551.495	543.205
644.048	527.023
829.85	288.826
1011.95	65.373

4.1.2.6 Oxidation

The oxidation model of FeCrAl cladding is based upon a parabolic rate law to determine the mass gain of oxide. The mass gain is then converted into an oxide thickness. The model presented here was developed for Kanthal APMT, which is one of the candidate ATF FeCrAl cladding alloys. The model was also developed for high temperature steam, resulting in low oxidation rates at normal operating temperatures. It is expected that oxidation of FeCrAl alloys will be negligible during normal operation, and that the model can be applied to the normal operating regime. The parabolic rate constant was determined by Pint et al. [63]:

$$k_p = k_o e^{-Q/T} \tag{4.16}$$

where k_p is the parabolic rate constant in units of g^2/cm^4-s, k_o is a constant equal to 7.84 g^2/cm^4-s, and Q is an activation energy in units of K with a value of 41373.7. The mass gain due to the oxide formation is then calculated by

$$w_g = k_p^{1/2} t^{1/2} \tag{4.17}$$

where w_g is the mass gain due to oxidation in units of mg/cm^2. Then the oxide thickness is determined by multiplying the mass gain by the conversion factor of 5.35 μm-(cm^2/mg), as proposed by Jönsson et al [64].

4.2 Normal Operating Conditions

4.2.1 LWR fuel rodlet demonstration problem with FeCrAl

In order to demonstrate the new FeCrAl modeling capabilities in BISON and to offer an initial assessment of the performance of FeCrAl claddings, we performed BISON simulations of a PWR fuel rodlet at typical operating powers. We considered C35M FeCrAl cladding with the models described in Section 4.1.2. Calculations with Zircaloy-4 cladding under analogous conditions were also performed in order to compare the behavior of the two cladding materials.

4.2.1.1 Setup of BISON simulations

A 2D axisymmetric analysis of a conceptual LWR fuel rodlet is considered. The assumed geometry, whose main parameters are reported in Table 4.6, includes a smeared column of ten UO_2 pellets, C35M FeCrAl cladding, an initial 80 μm pellet-clad gap, and an upper plenum. The radial clad thickness is set equal to 385 μm [16]. Note that the FeCrAl cladding is thinner than a Zircaloy cladding [14]. The adoption of a thinner clad is is necessary to reduce the neutronic penalty associated with the usage of FeCrAl as cladding material compared to Zr alloys, and would allow for an increased overall core fuel loading [14]. Using a thinner clad is thought to be possible both in view of the higher strength of FeCrAl [62] and its enhanced corrosion resistance [65].

Typical PWR operating conditions were used for this demonstration problem (e.g., see [2]). The rod power is assumed to rise linearly over three hours and is then held constant for 4 years at 25 kW/m. In addition to this base irradiation, an operational transient was considered in order to assess the impact of a power ramp on the performance of the FeCrAl cladding. In particular, after the 4-year irradiation at 25 kW/m, the power was increased to 40 kW/m (with a ramp rate of 6 kW/m/h) and held at this power for 48 hours. The finite element mesh employed in the simulations is shown in Fig. 4.4.

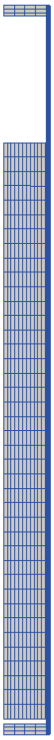

Figure 4.4: Finite element mesh for the LWR fuel rodlet demonstration problem. Note that a 2D axisymmetric problem is considered; hence, the left edge of the mesh represents the fuel centerline. The figure is scaled 2x along the radial direction for visualization.

In addition to the demonstration problem with FeCrAl, a corresponding case with Zircaloy was developed for comparison purposes (Section 4.2.1.3). The Zircaloy problem is analogous to the FeCrAl problem in terms of rod geometry and power conditions, with the exception of cladding thickness. This is set to a typical value for a PWR Zircaloy cladding of 575 μm [16], in order to provide a meaningful comparison. Correspondingly, the pellet radius is lower in the Zircaloy case, given an equal initial pellet-cladding gap for the two cases. The consdered geometries for the FeCrAl and Zircaloy cases are summarized in Table. 4.6.

4.2.1.2 Results and discussions for the FeCrAl demonstration problem

In this Section, the results of the BISON simulations of the LWR fuel rodlet demonstration problem with FeCrAl cladding are presented. In order to provide a sensitivity analysis of the effect of recently implemented models, four different input settings have been considered:

Table 4.6: Geometry of the LWR fuel rodlet demonstration problem. In addition to the case with FeCrAl, the geometry of a corresponding case with Zircaloy is summarized.

Cladding material	C35M	Zr–4
Cladding OD (mm)	9.50	9.50
Cladding thickness (μm)	385	575
Pellet–clad gap (μm)	80	80
Fuel material	UO_2	UO_2
Fuel stack length (mm)	118.6	118.6
Upper plenum length (mm)	26	26

- BISON originally available FeCrAl thermal and irradiation creep models from [57, 66]. Elastic fuel behavior is considered. (Blue lines in the figures below).

- New thermal creep model from [60] (Eq. 4.14), original irradiation creep model. Elastic fuel behavior is considered. (Dashed red lines).

- New thermal and irradiation creep models from [60] (Eqs. 4.14, 4.15). Elastic fuel behavior is considered. (Black lines).

- New thermal and irradiation creep models from [60] (Eqs. 4.14, 4.15). Fuel cracking and creep are considered. (Green lines).

Hence, in addition to the most recent FeCrAl models, in our sensitivity analysis we consider the impact of accounting for fuel cracking and creep (fourth setting). This is expected to affect cladding stresses and strains under fuel-cladding contact conditions, when fuel deformation affects cladding stress and diametral strain. Fuel cracking is represented using a newly implemented BISON model [67].

In Fig. 4.5, we plot the calculated hoop stress at the cladding inner radius and at fuel rod midplane as a function of time. The effects of the newly implemented creep and irradiation models are evident. In particular, note the lower stress obtained with the new thermal and irradiation creep models (black line) compared the original models (blue line), which is due to a higher creep rate and correspondingly higher stress relaxation. In particular, the impact of irradiation creep is remarkable. The effect of the new creep models is particularly evident during pellet-cladding contact conditions. Contact occurs in correspondence to the slope change for the stress curves, i.e., between 20000 and 25000 hours, depending on the considered setting. Contact occurs significantly earlier with the new irradiation creep correlation applied, which is due to more rapid creep-down of the cladding onto the fuel under the effect of outer coolant pressure.

The effect of considering fuel creep (visco-elastic behavior) and cracking is evident following fuel-cladding contact, with a lower stress in the cladding being calculated relative to the corresponding case with elastic fuel. This behavior is as expected, since fuel creep allows for the

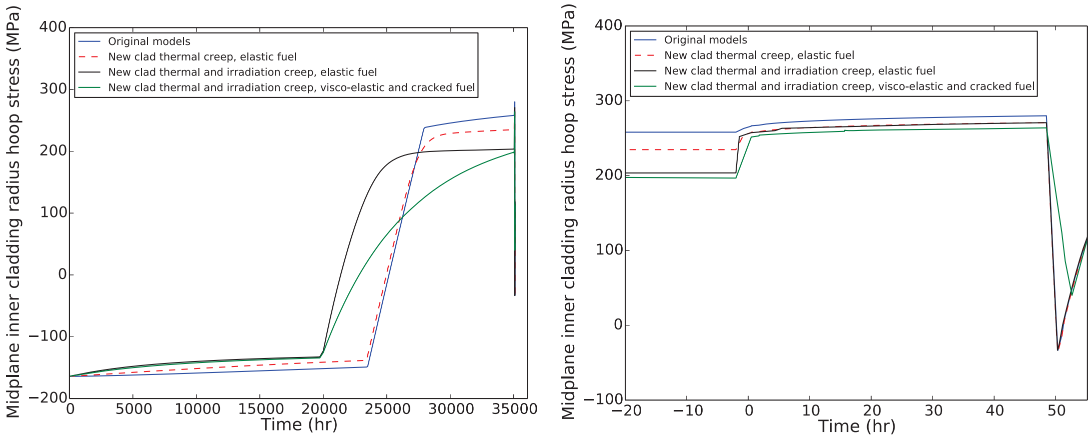

Figure 4.5: Calculated hoop stress at the cladding inner radius and fuel rod mid-plane from the BISON analyses of the FeCrAl demonstration problem. Sensitivity analysis is shown of the recently implemented models relative to the original models as in [57, 66]. Left: Full irradiation time. Right: Zoom on the power ramp and higher power period at the and of irradiation.

fuel to creep inwards under the mechanical restraint exerted by the cladding, resulting in lower cladding outward strain and tensile stress.

Following the power ramp to higher power, cladding stress increases due to fuel thermal expansion driving cladding outward strain.

It is interesting to note that the hoop stress remains below 300 MPa during the base irradiation and also the postulated operational transient (power ramp). These values are well below the ultimate tensile stress of the FeCrAl alloy at the considered temperatures (around 550 MPa [62]). Hence, the present results indicate that the FeCrAl cladding during LWR applications will undergo acceptable stresses during both steady-state operation conditions and operational transients.

In Fig. 4.6, we plot the calculated hoop strain at the cladding inner radius and at fuel rod midplane as a function of time. The new irradiation creep correlation (green and black lines) has the larger impact on the calculated cladding strain, which is consistent with the corresponding stress results presented in Fig. 4.5. When fuel-cladding contact occurs, the cladding strain is driven by fuel deformation. This is consistent with the blue, red and black lines having approximately the same slope (hence strain rate) during contact, despite the different cladding models. When considering creep and cracking in the fuel, the different fuel deformation rate results in different cladding strain rate. Under normal operating conditions, the strain in the C35M FeCrAl cladding is always below the rupture strain of the material (around 30% at the considered temperatures [62]).

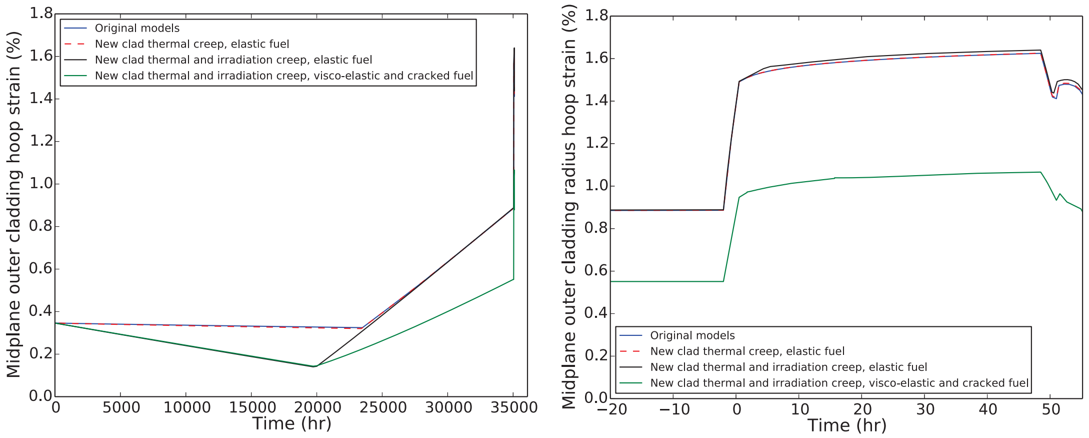

Figure 4.6: Calculated hoop strain at the cladding inner radius and fuel rod mid-plane from the BISON analyses of the FeCrAl demonstration problem. Sensitivity analysis is shown of the recently implemented models relative to the original models as in [57, 66]. Left: Full irradiation time. Right: Zoom on the power ramp and higher power period at the and of irradiation.

4.2.1.3 Comparison between FeCrAl and Zircaloy cladding behavior

In this Section, we present the results of a preliminary comparison of the behavior of FeCrAl and Zircaloy claddings for the LWR fuel rodlet demonstration problem.

As mentioned in Section 4.2.1.1, the Zircaloy case is analogous to the FeCrAl demo problem, with the cladding thickness being set to a typical value for a PWR Zircaloy cladding, in order to provide a meaningful comparison. The geometries for the FeCrAl and Zircaloy cases are summarized in Table. 4.6. The considered irradiation history is the same for the FeCrAl and Zircaloy cases and as described in Section 4.2.1.1, with a 4-year base irradiation at 25 kW/m followed by a power ramp and a holding time of 48 hours at 40 kW/m. For the FeCrAl case, we considered the setting with the most recent models as in Section 4.2.1.2, i.e., new clad thermal and irradiation creep, visco-elastic and cracked fuel. For the Zircaloy case, we also consider visco-elastic and cracked fuel, and the BISON models for Zircaloy as in [68].

Figure 4.7 reports the results of the BISON simulation in terms of cladding hoop stress at the rod mid-plane during the full irradiation (left) and the power ramp only (right). Fig. 4.8 reports the corresponding results in terms of cladding hoop strain.

First, the results point out that gap closure and fuel-cladding contact in the rod with the FeCrAl cladding occurs significanly later than in the rod with the Zircaloy cladding (Fig. 4.7, left, and Fig. 4.8, left). This is due to (i) a higher outward strain for the FeCrAl cladding after the initial rise to power, which is owing to the higher coefficient of thermal expansion of FeCrAl com-

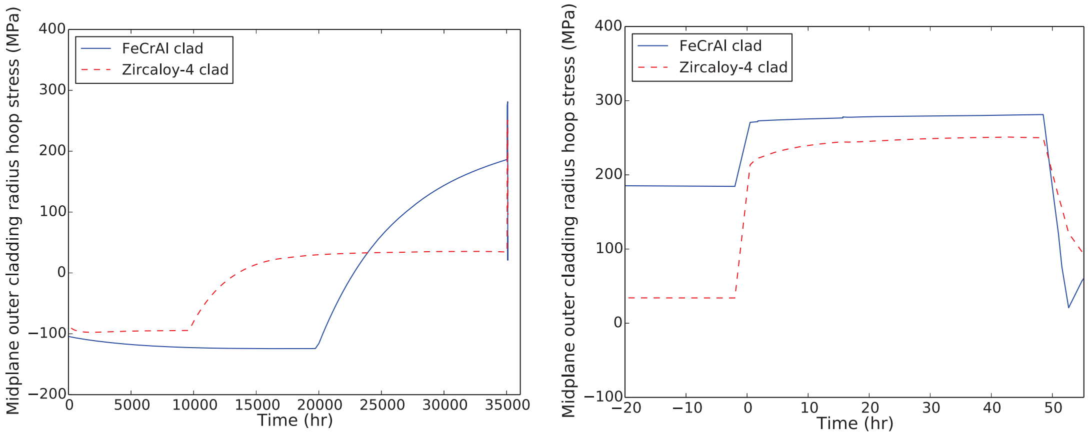

Figure 4.7: Comparison between the hoop stress in the FeCrAl cladding and in the Zircaloy cladding for the LWR demonstration problem analyzed with BISON. The hoop stress at the cladding inner radius and fuel rod mid-plane is considered. Left: Full irradiation time. Right: Zoom on the power ramp and higher power period at the and of irradiation.

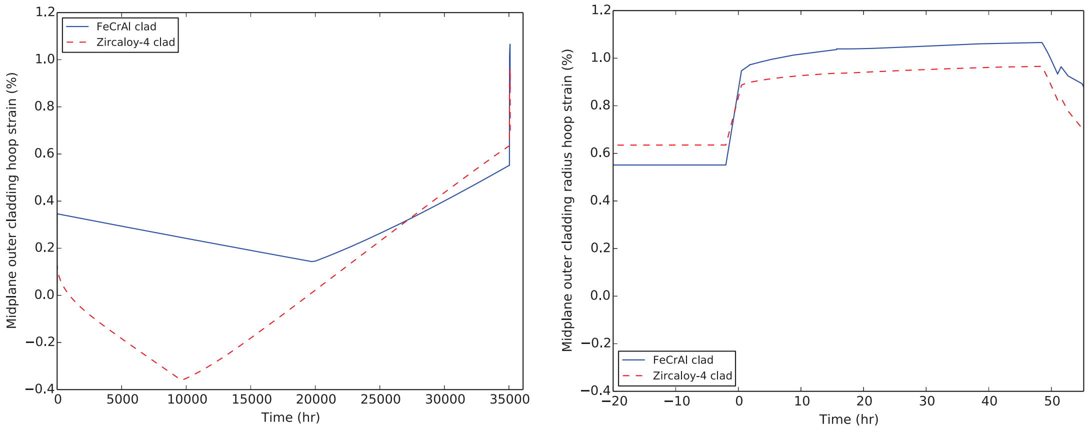

Figure 4.8: Comparison between the hoop strain in the FeCrAl cladding and in the Zircaloy cladding for the LWR demonstration problem analyzed with BISON. The hoop strain at the cladding inner radius and fuel rod mid-plane is considered. Left: Full irradiation time. Right: Zoom on the power ramp and higher power period at the and of irradiation.

pared to Zircaloy (Table 4.3), and (ii) a lower rate of creep-down of the FeCrAl cladding under coolant pressure due to the lower creep rate of the FeCrAl alloy compared to Zircaloy at a given temperature. Both effects are evident in Fig. 4.8, left.

The cladding hoop stress is negative (compressive) due to outer coolant pressure in open gap conditions, and becomes positive (tensile) following fuel-cladding contact. Apart from the compression-to-tension transition periods, the absolute stress in the FeCrAl cladding is higher than in the Zircaloy cladding (Fig. 4.7, left). This is expected in view of the lower thickness of the FeCrAl cladding as well as the lower rate of stress relaxation due to creep. However, the calculated stress in the FeCrAl cladding is well below the FeCrAl ultimate tensile strength (i.e., around 550 MPa at the temperature characteristic of the cladding [62]) during the whole irradiation, including the final power ramp.

The strain plot in Fig. 4.8, left, points out the lower strain rate due to creep in the FeCrAl cladding relative to the Zircaloy cladding, both during the creep-down period and the outward creep period following contact. The higher strain in the FeCrAl cladding than in the Zircaloy cladding during the power ramp (Fig. 4.8, right), instead, is due to the the higher coefficient of thermal expansion of FeCrAl (Table 4.3).

In short, the present comparison between the behavior of a C35M FeCrAl alloy and a Zircaloy cladding under analogous conditions representative of PWR normal operating conditions points out that:

- Due to the higher thermal expansion and lower creep rate of the FeCrAl cladding, gap closure and fuel-cladding contact are delayed compared to the Zircaloy cladding.

- Once fuel-cladding contact occurs, cladding outward strain rate is lower for the FeCrAl cladding, due to the lower creep rate relative to Zircaloy, under steady-state conditions. During a power ramp, the FeCrAl cladding can undergo a higher outward strain associated with higher thermal expansion.

- The FeCrAl cladding is generally subject to higher stresses than the Zircaloy cladding, which is due to a lower wall thickness and a lower creep rate of the material at a given temperature. However, the stress in the FeCrAl cladding remains well below the FeCrAl ultimate tensile strength during steady-state operation and a postulated operational transient.

4.2.2 LWR fuel rodlet demonstration problem with U_3Si_2

Utilizing the same finite element mesh and power history as used in the FeCrAl LWR fuel rodlet demonstration in the previous section, comparative simulations were completed between UO_2 and U_3Si_2 fueled rodlets both clad in Zircaloy-4. The material models for U_3Si_2 used in this analysis were described in detail in the previous section including temperature dependent thermal conductivity and specific heat, constant Young's modulus, Poisson's ratio, and thermal expansion, and burnup-dependent solid and gaseous swelling. Since the development of a U_3Si_2 fission gas release model is in its infancy, the Simple Integrated Fission Gas Release and Swelling (SIFGRS) model for UO_2 was also used for U_3Si_2 in absence of other data. In the rodlet containing UO_2 fuel, the material and behavior models included were burnup and temperature dependent thermophysical properties, fuel creep, solid and gaseous swelling, densification, relocation, and fission gas release.

Figure 4.9a illustrates the fuel centerline, fuel surface, and cladding inner surface temperatures for both rodlets. The highter thermal conductivity of U_3Si_2 results in a centerline temperature is approximately 400 K lower than observed for UO_2. Consequently, the lower operating temperature result in less thermal expansion, and the fuel-to-clad gap remains open longer. The burnup at which gap closure occurs is when the slope of the temperature curves abruptly change. UO_2 has a lower fuel surface temperature early in life because relocation results in a large diametrical strain that reduces the fuel-to-clad gap. The lower fuel temperatures in U_3Si_2 also results in no fission gas being released. Zero released fission gas coupled with the larger overall internal volume due to no relocation in the U_3Si_2 rodlet results in a lower plenum pressure as illustrated in Figure 4.9b. It was observed that the achieved burnup for the same irradiation history was lower in the U_3Si_2rodlet. This is due to the higher uranium density in U_3Si_2 compared to UO_2.

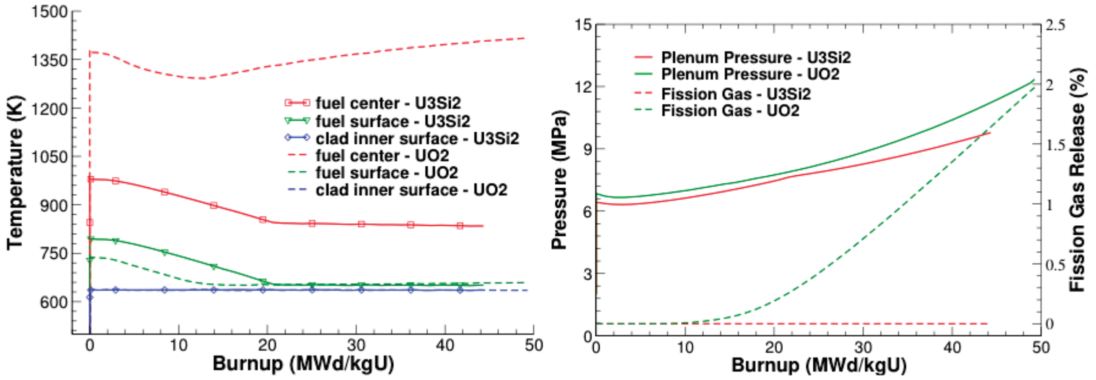

(a) (b)

Figure 4.9: Comparisons between using U_3Si_2 and UO_2 in the example problem (a) fuel centerline, fuel surface, and clad inner surface temperatures, (b) plenum pressure and fission gas release.

4.3 Accident Conditions

The response of U_3Si_2 fuel and FeCrAl cladding under postulated accident conditions including Loss of Coolant, Station Blackout and Reactivity Insertion. Discrete ten pellet rodlets were used for the LOCA and SBO scenarios (both U_3Si_2/Zircaloy-4 and UO_2/FeCrAl). The RIA was applied to a full length rod of U_3Si_2 fuel clad with Zircaloy.

4.3.1 Loss of Coolant Accident

Three ten pellet rodlets (UO_2/Zircaloy, U_3Si_2/Zircaloy-4, UO_2/FeCrAl) based upon a modified version of the BISON example problem were compared under postulated LOCA conditions to investigate how the ATF concepts behave relative to rods currently used in LWRs. To enable comparisons between the different rodlets, the initial rod diameter (cladding outer diameter) and cold fuel-to-cladding gap are the same in all cases. The cladding thickness is varied depending on whether the material is Zircaloy-4 or FeCrAl to simulate the thinner cladding required when FeCrAl is used to overcome the neutronic penalty. To compensate for the thinner cladding, the pellet diameter was increased for the UO_2/FeCrAl rodlet. The specifications of the fuel rodlets are summarized in Table 4.7.

Table 4.7: Specifications for the three rodlets

	UO_2/Zircaloy-4 Rodlet	**U_3Si_2/Zircaloy-4 Rodlet**	**UO_2/FeCrAl Rodlet**
Number of pellets	10	10	10
Pellet length (mm)	9.83	9.83	9.83
Pellet outer diameter (mm)	8.1915	8.1915	8.1915
Dish depth (mm)	0.3	0.3	0.3
Chamfer width (mm)	0.5	0.5	0.5
Chamfer height (mm)	0.16	0.16	0.16
Radial gap width (μm)	82.55	82.55	82.55
Clad thickness (mm)	0.5715	0.5715	0.35
Rodlet length (mm)	107.203	107.203	107.203
Rodlet diameter (mm)	9.4996	9.4996	9.4996
Initial fill pressure (MPa)	2.0	2.0	2.0
Initial fill gas	Helium	Helium	Helium
Initial grain size (μm)	20	20	20
Coolant inlet mass flux (kg m^{-2} s^{-1})	10	10	10
Coolant inlet temperature (K)	583	583	583
Coolant pressure (MPa)	15.5	15.5	15.5

Prior to the LOCA transient a nominal base irradiation was prescribed to the rodlets. The base irradiation is shown in Figure 4.10. A flat axial profile was assumed for these short rodlets. The LOCA begins at 80050000 seconds (~926.5 days) for all rodlets. The burnup at the beginning of the LOCA for the UO_2/Zircaloy-4 and UO_2/FeCrAl rodlets was 53 MWd/kgU and was 47.67 MWd/kgU for the U_3Si_2/Zircaloy-4 rodlet. To simulate the LOCA, the 1-D coolant channel model's inlet mass flux was dropped to 1 kg/m^2/s and the coolant pressure reduced to atmospheric over 10 seconds, thereby significantly reducing the cladding-to-coolant heat transfer coefficient. This type of scenario is representative of a Large Break LOCA. Meanwhile the power supplied to the fuel was dropped to zero over two seconds at which time decay heat is turned on as a source term. The LOCA was terminated after 90 seconds due to numerical instabilities likely due to large cladding strains. Reflood (quenching) was not simulated.

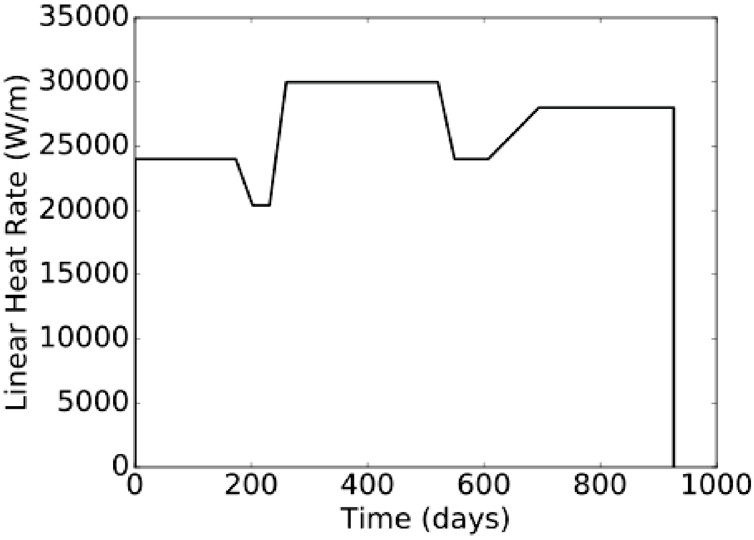

Figure 4.10: Base irradiation power history.

Due to the lack of experimental data and limited knowledge of the fuel performance response of the accident tolerant fuel concepts under postulated LOCA conditions, sensitivity analyses can be used to provide additional insight. There are numerous statistical methodologies available to determine the sensitivity of the output metrics of interest to uncertainties in select input parameters including Pearson and Spearman correlation coefficients, main effects studies, surrogate models, and variance based decomposition. Here, BISON is coupled to the DAKOTA [69] sensitivity analysis software to perform main effects studies that illustrate the importance of uncertain input parameters on the fuel centerline temperature and total cladding hoop strain at the end of the transients for the UO_2/FeCrAl and U_3Si_2/Zircaloy-4 rodlets. The input parameters of interest in this study are presented in Table 4.8 for the UO_2/FeCrAl rodlet and Table 4.9 for the U_3Si_2/Zircaloy-4 including their maximum, minimum and mean values. Note that the creep correlations are scaled by orders of magnitude because it is expected that C35M will creep more than the current commercial FeCrAl alloys at higher temperatures. GB and IG stand for grain boundary and intergranular, respectively. These diffusion coefficients are varied in the U_3Si_2/Zircaloy-4 case due to the limited knowledge of fission gas behavior in silicide fuel.

Table 4.8: Parameters varied in the main effects analysis including their minimum, mean, and maximum values for the UO_2/FeCrAl rodlet.

	Minimum	**Mean**	**Maximum**
Thermal creep scaling factor	1.0	50.5	100.0
Irradiation creep scaling factor	1.0	5.5	10.0
Volumetric swelling scaling factor	0.8	1.0	1.2
Young's modulus scaling factor	0.8	1.0	1.2
Fuel enrichment (%)	5	6.5	8

Table 4.9: Parameters varied in the main effects analysis including their minimum, mean, and maximum values for the U_3Si_2/Zircaloy-4 rodlet.

	Minimum	**Mean**	**Maximum**
GB diffusion coefficient scaling factor	1.0	5000.0	10000.0
IG diffusion coefficient scaling factor	1.0	5000.0	10000.0
Thermal conductivity scaling factor	0.8	1.0	1.2
Gas swelling scaling factor	0.8	1.0	1.2
Specific heat capacity scaling factor	0.95	1.0	1.05

The results of the LOCA simulations are presented in Figures 4.11, 4.12, and 4.13. Figure 4.11 highlights the comparison between the three systems for the baseline cases. In these cases the uncertain material parameters are taken as their default values. The plots show the evolution of the fuel centerline temperature and cladding hoop strain during the LOCA (i.e., t = 0 is the end of the base irradiation). The rapid decrease in the fuel centerline temperature at the beginning of the LOCA is due to the removal of power to the fuel. Once the mass flux has decreased to its very small minimum value at 10 s the temperature begins to rise due to the decay heat and severely degraded heat transfer coefficient. It is observed that the two ATF systems result in lower centerline temperature at the end of the 90 s transient. The strain evolution in Figure 4.11b clearly illustrates the significant hoop strain experienced by Zircaloy during the LOCA. The sharp transition in the UO_2 case at 10 s corresponds to the significant reduction in heat transfer on the surface of the cladding. Both the UO_2/Zircaloy-4 and U_3Si_2/Zircaloy-4 cases begin following an exponential increase in strain due to the significant deformation experienced by Zircaloy during the LOCA. The UO_2/FeCrAl observes superior performance in terms of cladding deformation, as the strain remains very low.

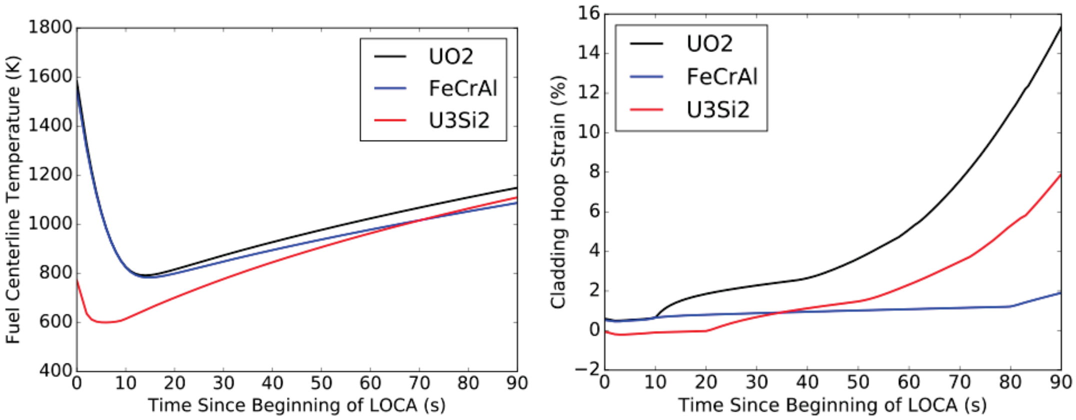

(a) **(b)**

Figure 4.11: Comparison of the (a) centerline temperature and (b) cladding hoop strain during for the three fuel systems during a LOCA transient.

Figure 4.12 illustrates the main effects plots for the UO_2/FeCrAl system during the LOCA transient. In a main effects study the output metric of interest (e.g., centerline temperature) is shown on the ordinate axis, whereas the various input parameters are plotted along the abscissa. Each subplot in a particular diagram represents the main effects of that input parameter. To provide guidance on how to interpret the results of a main effects study initially focus on the swelling scale factor subplot in Figure 4.12a. The point for a swelling scale factor of 0.8 represents the mean centerline temperature for all of the simulations that had the swelling scale factor set to 0.8. A monotonic upward slope when an input variable is varied indicates a positive correlation with the output metric. Subsequently, a monotonic downward slope represents a negative correlation between the input parameter and output metric. Lines that are close to horizontal imply no correlation between input and output. Note that all of the data points represent the mean values at the last timestep of the transient, but the DAKOTA analysis was applied to the entire irradiation history.

For the UO_2/FeCrAl system the main effects study highlights the importance of the swelling scaling factor and the fuel enrichment. The centerline temperature and cladding hoop strain are both positively correlated with the swelling strain. Contrarily, the fuel enrichment is negatively correlated with centerline temperature but positively correlated with the hoop strain. Higher enrichment leads to a larger burnup within the fuel, particularly in the rim region at the periphery of the pellet. The swelling correlation in BISON is burnup dependent, thus, increased enrichment results in larger fuel swelling. Larger fuel swelling results in contact between the fuel and cladding earlier in the LOCA transient resulting in a decreased centerline temperature. Subsequently, the harder the contact occurring between the fuel and cladding the larger the strain. Interestingly, the large scaling factors on the thermal and irradiation creep appear to have no influence, indicating that the creep strain is still significantly low. It is prudent to note that the range of centerline temperature and cladding hoop strain is small.

The results of the main effects study for the U_3Si_2/Zircaloy-4 system during the LOCA are shown in Figure 4.13. In this case the range of the output metrics is much larger than the UO_2/FeCrAl system indicating that uncertainty in U_3Si_2behavioral models have a more significant impact on the centerline temperature and hoop strain. As expected the significant uncertainty assumed on the intergranular diffusion coefficient results in large variations in the centerline temperature and cladding hoop stress. The larger diffusion coefficients give rise to increased stress due to greater fission gas release to the plenum increasing the internal pressure and inducing larger stress on the cladding. In addition, increasing the thermal conductivity results in lower temperatures and strains. Surprisingly, uncertainty in the specific heat capacity has a significant correlation with the centerline temperature for such a long duration transient. Usually, the specific heat only has an affect during very short duration transients (e.g., reactivity insertion accidents). The plots indicate that the grain boundary diffusion coefficient and gaseous swelling have minimal effects. It is anticipated that at very high burnups (>60 MWd/kgU) gaseous swelling would be the most dominant behavior due to the rapid increase in gaseous swelling at high burnups. In this study the burnup after the base irradiation was approximately 5.01% FIMA (47.67 MWd/kgU) which is just above the threshold for gaseous swelling of 5% FIMA in the current BISON model.

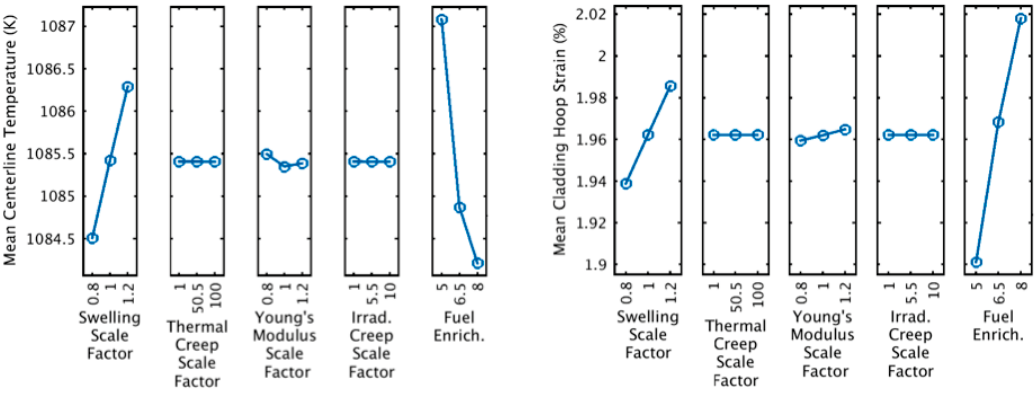

(a) (b)

Figure 4.12: Main effects plots for the UO_2/FeCrAl rodlet at the end of the LOCA transient.

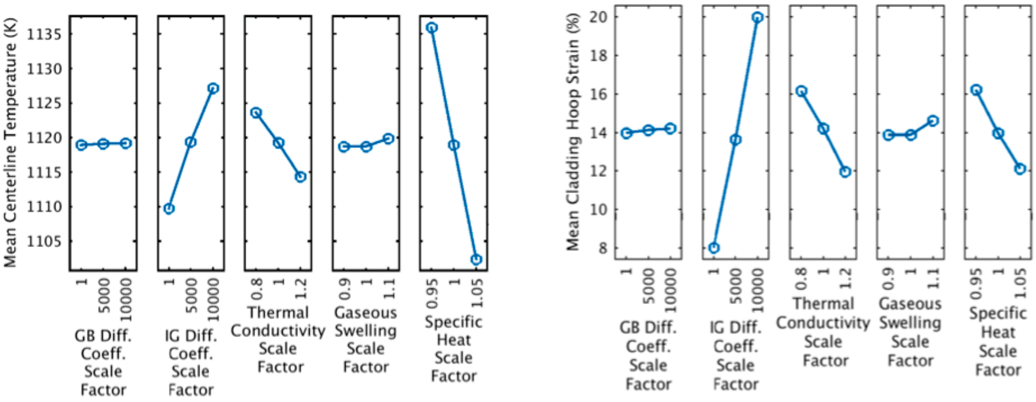

(a) (b)

Figure 4.13: Main effects plots for the U_3Si_2/Zircaloy-4 rodlet at the end of the LOCA transient.

4.3.2 Station Blackout

The three rodlets that were subjected to the LOCA in the previous section were also subjected to a postulated station blackout scenario at the conclusion of the base irradiation illustrated in Figure 4.10. To simulate the SBO after the base irradiation, the coolant pressure was kept at 15.5 MPa while the coolant flow was drecreased to 100 kg/m^2/s to simulate the minimal flow rate introduced by the backup cooling system over 10 s. The power was shut off over 2 seconds and decay heat turned on as a source term. As with the LOCA case, baseline comparisons and main effects studies were performed for the station blackout. The duration of the SBO was 24 hours.

The results of the SBO simulations are presented in Figures 4.14, 4.15 and 4.16. Figure 4.14 presents the comparison between the three systems for the baseline cases. The plots show the evolution of the fuel centerline temperature and cladding hoop strain during the station blackout transient. For the SBO plots, the beginning of the transient (t=0) in the plot is taken as the time when the cooling water mass flux equals 100 kg/m^2/s. This value represents the minimal flow provided by the backup cooling system. It is observed that the centerline temperature approaches the coolant inlet temperature rapidly. This can be attributed to the size of the rodlet considered. The coolant channel model takes the bottom of the rodlet as the inlet and because the rodlet is only 107.2 mm long it can still be cooled quickly with minimal coolant flow. Subsequently, because the fuel and cladding temperatures remain low, the stress induced in the cladding is minimal. Thus, simulations of full-length fuel rods are required to provide conclusive qualitative comparisons of the three systems during a station blackout event. It should be noted that the reduced flow decreases the rate of cooling from full power.

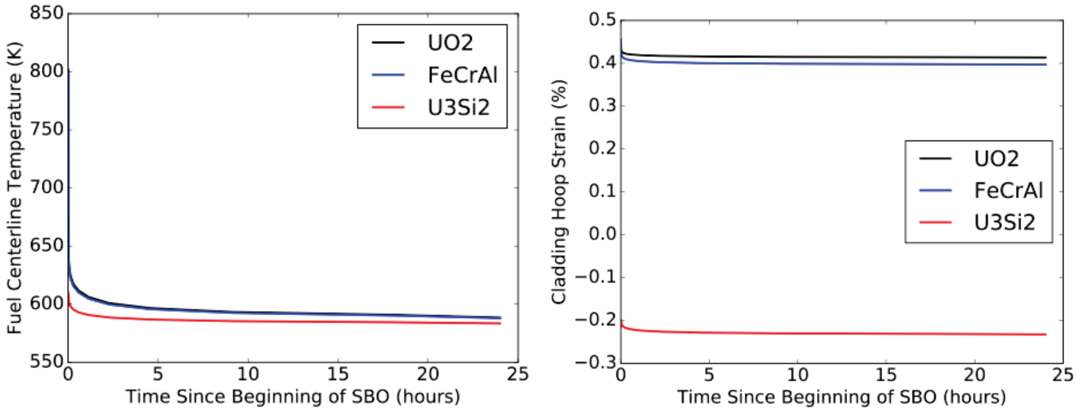

(a) (b)

Figure 4.14: Comparison of the (a) centerline temperature and (b) cladding hoop strain for the three fuel systems during a postulated SBO transient.

The UO$_2$/FeCrAl system's main effects study for the SBO scenario is shown in Figure 4.15. Since the temperatures in the baseline cases approach the coolant inlet temperature, expectations of much variation during the SBO scenario were low. However, it was found that the cladding hoop strain had strong positive correlations between the Young's modulus and swelling factor. Comparing this to the LOCA case it can be concluded that at the end of the SBO there is no contact between the fuel and cladding because the Young's modulus correlates with the strain. Whereas, in the LOCA case shown previously, the Young's modulus has no effect, indicating contact had been established at the end of the transient.

The U$_3$Si$_2$/Zircaloy-4 system experienced a minute variation in the centerline temperature and cladding hoop strain with respect to the uncertainties in the inputs for the SBO case as shown in Figure 4.16. Strong correlations are still observed for the intergranular diffusion coefficient and thermal conductivities. An important observation is that for the SBO transient, which lasted 24

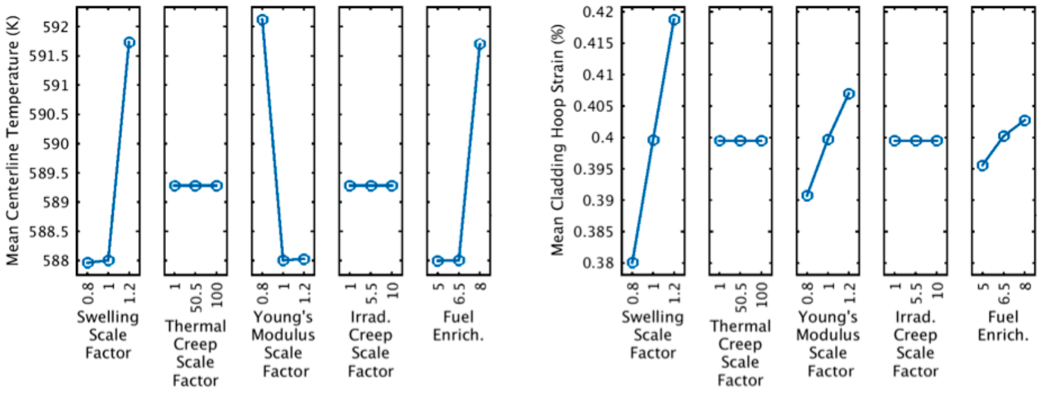

(a) **(b)**

Figure 4.15: Main effects plots for the UO_2/FeCrAl rodlet at the end of the SBO transient.

hours, compared to the LOCA that lasted 90 seconds, the specific heat has no correlation with the output parameters. This is expected for the long duration transients.

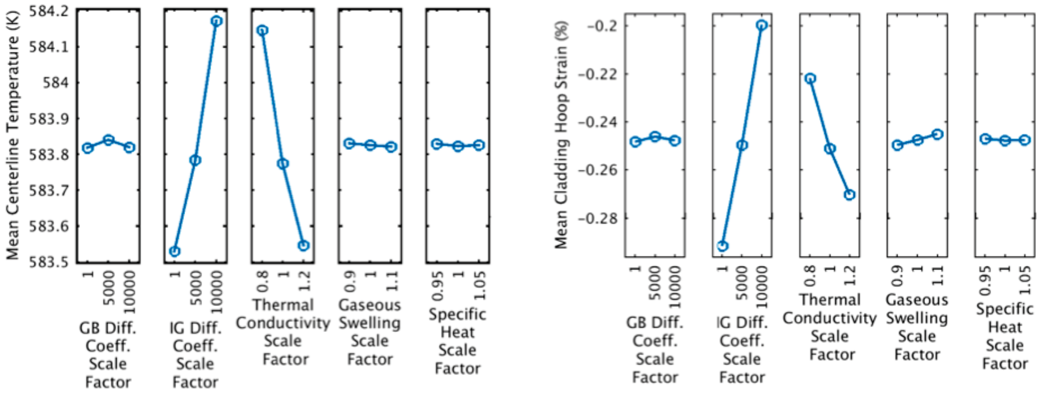

(a) **(b)**

Figure 4.16: Main effects plots for the U_3Si_2/Zircaloy-4 rodlet at the end of the SBO transient.

4.3.3 Reactivity Insertion Accident

In fiscal year 2016 a Reactivity Insertion Accident (RIA) was analyzed in collaboration with colleagues at Brookhaven National Laboratory. In this study a different simulation domain was used compared to the LOCA and SBO scenarios discussed previously. The full details of the analysis are provided in a TopFuel 2016 paper accepted for presentation as a poster at the meeting [70]. In brief, a RIA was simulated on fresh fuel from hot full power conditions (33658

W/m) for two rod systems: UO_2/Zircaloy-4 and U_3Si_2/Zircaloy-4. The rods had dimensions of an AP-1000 fuel rod. The poster history and axial power profile were generated using the TRACE [71] and PARCS [72] codes, respectively. Since the BISON coolant channel model is not currently developed to handle the complex coolant conditions during a RIA, the cladding outer surface temperature was provided as a Dirichlet boundary conditions in BISON, obtained from TRACE. The reactivity insertion corresponded to a $1 ramp. Figure 4.17 presents the normalized reactoer power calculated by TRACE and the core-averaged axial power distribution calculated by PARCS The normalized reactor power is converted to average linear heat rate in units of W/m for use in BISON. The simulations of the two rod systems were terminated after 1 second.

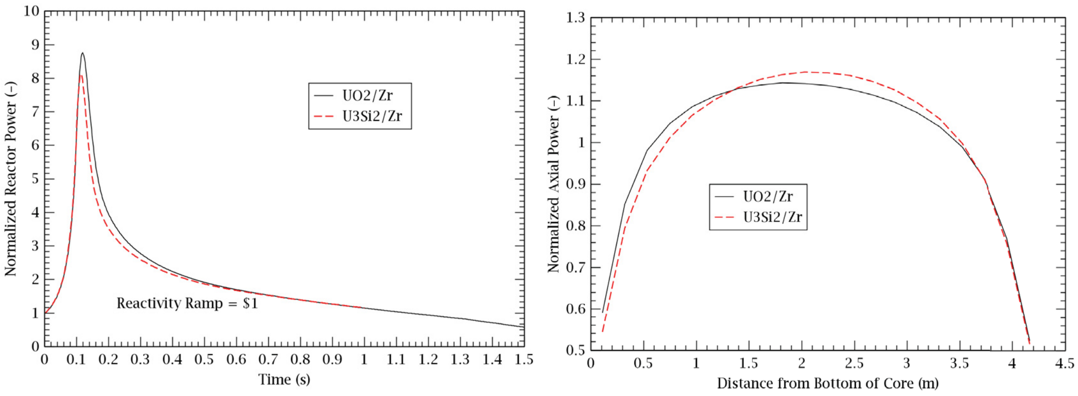

(a) **(b)**

Figure 4.17: Illustration of the (a) normalized power history calculated by TRACE and (b) axial power profile calculated by PARCS applied to the UO_2/Zircaloy-4 and U_3Si_2/Zircaloy-4 rods for the RIA scenario.

A code-to-code comparison was completed between BISON and TRACE for the fuel centerline temperature for both rods. Figure 4.18 presents the axial temperature variation at simulation times of 0.0 (start of RIA), 0.2 and 0.6 s. The difference between the BISON and TRACE simulations are due to the gap conductance and thermal expansion models used by the codes. The important observation to make when comparing Figure 4.18a and 4.18b is that the centerline temperature is consistently lower for the U_3Si_2/Zircaloy-4 rod. This preliminary conclusion is a positive argument for using U_3Si_2 as an accident tolerant fuel. However, the melting temperature of U_3Si_2 is lower than that for UO_2, reducing the net benefit.

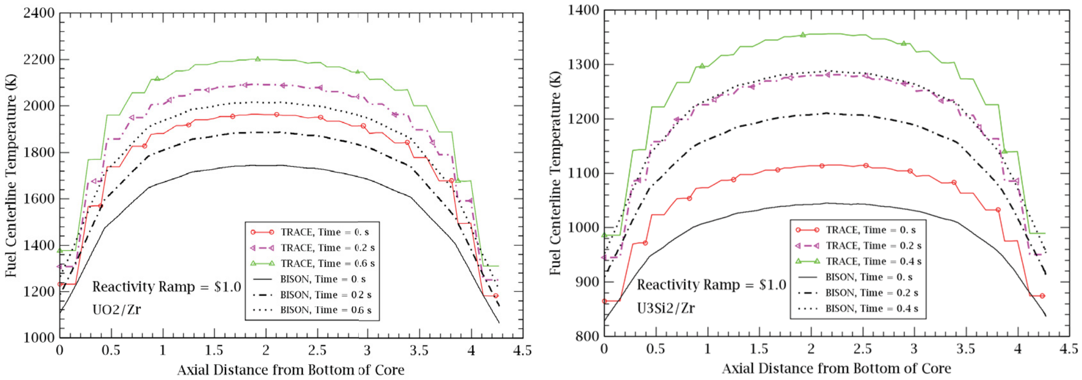

(a) **(b)**

Figure 4.18: Axial temperature profile during the RIA for (a) the UO_2/Zircaloy-4 and (b) the U_3Si_2/Zircaloy-4 rods at times of 0.0, 0.2 and 0.6 s.

5 Summary

In response to the events that occurred at the Fukushima-Daiichi nuclear power plant in March of 2011, the US DOE through its NEAMS program have funded an ATF HIP. The ATF HIP is a multi laboratory and university effort to investigate two proposed accident tolerant materials: U_3Si_2 fuel and FeCrAl cladding, using a multiscale multiphysics approach. This report provides a brief overview of the lower length scale efforts that are underway in support of the engineering scale models to be included in the BISON fuel performance code. The laboratory and contributors to the work were provided. Next, a description of the material models for U_3Si_2 and FeCrAl that have been introduced into BISON was provided. The material models are under constant modification as new experimental data becomes available and additional lower length scale work is completed. The application of these models to normal operating and accident conditions was summarized. The preliminary results indicate that the accident tolerant concepts perform as good or better under normal operating and accident conditions as the standard fuel system. However, additional research is required in important areas where data is limited, such as fission gas release in U_3Si_2 and irradiation creep in FeCrAl.

6 Future Work

Although the behavioral response of two proposed accident tolerant fuel concepts has been explored in this report, further work at the engineering scale is required going into the final year of the HIP. First, the normal operating power history was a representative power history that was generated to achieve appreciable burnup. For an improved understanding of the behavior of the ATF concepts under LWR conditions, an actual power history in a commercial LWR reactor should be used. The next step is to perform the analyses shown in this report using the power history for the TSQ002 rod in the US PWR 16x16 experiment that was irradiated in a US commercial pressurized water reactor (PWR) [73]. Moreover, additional model improvements for U_3Si_2 and FeCrAl are desired. Extensions of the normal operating and accident analyses including the breadth of sensitivity analyses completed are planned.

For U_3Si_2 fuel future goals include:

- Inclusion of radiation damage degradation in the Zhang thermal conductivity model and the Miao gaseous swelling model.
- Continue development of a fission gas release model.
- Finalization of the implementation of the radial power profile for U_3Si_2 obtained from neutronics calculations.
- Incorporate the Zhang and Miao models into the normal operating and accident condition investigations.

For FeCrAl cladding future goals include:

- Updating the thermal and irradiation creep models for FeCrAl as experimental data becomes available.
- Incorporating the lower length scale VPSC model under development at LANL into BISON.
- Utilizing the recently added FeCrAl burst model in the accident condition investigations.

For the application of the ATF concepts to normal operating and accident conditions future goals include:

- Performing more simulations on full length rods.
- Applying a more justifiable base irradiation history such as that of the TSQ002 rod irradiated in a commercial PWR.
- Investigating late life power ramps.
- Comparing cladding stresses between smeared and discrete pellet cases.
- Performing coupling analyses with a system code such as RELAP-7 for improved treatment of the coolant boundary conditions under transient conditions.
- Extending the sensitivity analyses to include variance-based indices (e.g., polynomial regression or polynomial chaos expansions) that provide additional detail into which model parameters are of greatest importance.
- Extending sensitivity analyses to include reactivity insertion accidents.

7 Acknowledgements

Funding for this work is from the DOE Nuclear Energy Advanced Modeling and Simulation program through the Accident Tolerant Fuel High Impact Problem. The submitted manuscript has been authored by a contractor of the U.S. Government under Contract DE-AC07-05ID14517. Accordingly, the U.S. Government retains a non-exclusive, royalty free license to publish or reproduce the published form of this contribution, or allow others to do so, for U.S. Government purposes.

Bibliography

[1] S. Bragg-Sitton, B. Merrill, M. Teague, L. Ott, K. Robb, M. Farmer, M. Billone, R. Montgomery, C. Stanek, M. Todosow, and N. Brown. Advanced fuels campaign: enhanced LWR accident tolerant fuel performance metrics. Technical Report INL/EXT-13-29957, Idaho National Laboratory, 2013.

[2] R. L. Williamson, J. D. Hales, S. R. Novascone, M. R. Tonks, D. R. Gaston, C. J. Permann, D. Andrs, and R. C. Martineau. Multidimensional multiphysics simulation of nuclear fuel behavior. *Journal of Nuclear Materials*, 423:149–163, 2012.

[3] J. D. Hales, R. L. Williamson, S. R. Novascone, D. M. Perez, B. W. Spencer, and G. Pastore. Multidimensional multiphysics simulation of TRISO particle fuel. *Journal of Nuclear Materials*, 443:531–543, 2013.

[4] J. D. Hales, S. R. Novascone, B. W. Spencer, R. L. Williamson, G. Pastore, and D. M. Perez. Verification of the BISON fuel performance code. *Annals of Nuclear Energy*, 71:81–90, 2014.

[5] M. R. Tonks, D. Gaston, P. C. Millett, D. Andrs, and P. Talbot. An object-oriented finite element framework for multiphysics phase field simulations. *Computational Materials Science*, 51:20–29, 2012.

[6] J.T. White, A.T. Nelson, J.T. Dunwoody, D.D. Byler, D.J. Safarik, and K.J. McClellan. Thermophysical properties of U_3Si_2 to 1773 k. *Journal of Nuclear Materials*, 464:275–280, 2015.

[7] J. M. Harp, L. He, R. E. Hogan, and A. R. Wagner. Corrosion and interdiffusion studies of U_3Si_2. In *Proceedings of TopFuel*, Boise, ID, USA, 2016.

[8] E. S. Wood, J. T. White, D. D. Byler, and A. T. Nelson. The synthesis and air oxidation behavior of U-Si-Al and U-Si-B compositions. In *Proceedings of TopFuel*, Boise, ID, USA, 2016.

[9] J. T. White, E. S. Wood, J. T. Dunwoody, and A. T. Nelson. State of knowledge and challenges of U-Si compounds for use in light water reactor accident tolerant fuel designs. In *Proceedings of TopFuel*, Boise, ID, USA, 2016.

[10] D. T. Goddard, D. P. Mathers, D. G. Eaves, P. Xu, E. J. Lahoda, and J. M. Harp. Manufacturability of U_3Si_2 and its high temperature oxidation behavior. In *Proceedings of TopFuel*, Boise, ID, USA, 2016.

[11] M.R. Finlay, G.L. Hofman, and J.L. Snelgrove. Irradiation behaviour of uranium silicide compounds. *Journal of Nuclear Materials*, 325:118–128, 2004.

[12] K. E. Metzger, T. W. Knight, and R. L. Williamson. Model of U_3Si_2 fuel system using BISON fuel code. In *Proceedings of the International Congress on Advances in Nuclear Power Plants, 2014*, Charlotte, NC, USA, 2014.

[13] R. E. Stachowski, R. B. Rebak, W. P. Gassmann, and J. Williams. Progress of GE development of accident tolerant fuel FeCrAl cladding. In *Proceedings of TopFuel*, Boise, ID, USA, 2016.

[14] K. A. Terrani, S. J. Zinkle, and L. L. Snead. Advanced oxidation-resistant iron-based alloys for LWR fuel cladding. *Journal of Nuclear Materials*, 448:420–435, 2014.

[15] Xunxiang Hu, Kurt A. Terrani, Brian D. Wirth, and Lance L. Snead. Hydrogen permeation in fecral alloys for LWR cladding application. *Journal of Nuclear Materials*, 461:282–291, 2015.

[16] Caleb P. Massey, Kurt A. Terrani, Sebastien N. Dryepondt, and Bruce A. Pint. Cladding burst behavior of Fe-based alloys under LOCA. *Journal of Nuclear Materials*, 470:128–138, 2016.

[17] E. Lahoda, S. Ray, F. Boylan, P. Xu, and R. Jacko. SiC cladding corrosion and mitigation. In *Proceedings of TopFuel*, Boise, ID, USA, 2016.

[18] Weon-Ju Kim, Daejong Kim, and Ji Yeon Park. Fabrication and material issues for the application of SiC composites to LWR fuel cladding. *Nuclear Engineering and Technology*, 45(4):565–572, 2013.

[19] Yutai Katoh, Lance L. Snead, Ting Cheng, Chunghao Shih, W. Daniel Lewis, Takaaki Koyanagi, Tatsuya Hinoki, Charles H. Henager Jr., and Monica Ferraris. Radiation-tolerant joining technologies for silicon carbide ceramics and composites. *Journal of Nuclear Materials*, 448(13):497–511, 2014.

[20] J. Bischoff, C. Vauglin, C. Delafoy, P. Barberis, D. Perche, B. Guerin, J.-P. Vassault, and J.-C. Brachet. Development of Cr-coated zirconium alloy cladding for enhanced accident tolerance. In *Proceedings of TopFuel*, Boise, ID, USA, 2016.

[21] Kurt A. Terrani, Lance L. Snead, and Jess C. Gehin. Microencapsulated fuel technology for commercial light water and advanced reactor application. *Journal of Nuclear Materials*, 427(13):209–224, 2012.

[22] Y. Zhang, D. Schwen, L. Aagesen, K. Ahmed, and J. Yu. Overview of lower length scale model development for accident tolerant fuels regarding U_3Si_2 and FeCrAl cladding. Technical Report INL/EXT-16-40010, Idaho National Laboratory, 2016.

[23] M. J. Noordhoek, T. M. Besmann, D. Andersson, S. C. Middleburgh, and A. Chernatynskiy. Phase equilibria in the U-Si system from first-principles calculations. *Journal of Nuclear Materials*, 479:216–223, 2016.

[24] M. J. Noordhoek, D. Andersson, and T. M. Besmann. Structure determination and stability for Pa-Si, Np-Si and U-X-Si (X=Mo, Th, Np) phases from first-principles. *Journal of Nuclear Materials*, 479:593–607, 2016.

[25] M. J. Middleburgh, R. W. Grimes, E. J. Lahoda, C. R. Stanek, and D. A. Andersson. Stoichiometry deviation in U_3Si_2. *Journal of Nuclear Materials*, submitted.

[26] Xunxiang Hu, Donghua Xu, and Brian D. Wirth. Quantifying he-point defect interactions in fe through coordinated experimental and modeling studies of he-ion implanted single-crystal fe. *Journal of Nuclear Materials*, 442(13, Supplement 1):S649–S654, 2013. Fifteenth International Conference on Fusion Reactor Materials.

[27] Brian D. Wirth, Xunxiang Hu, Aaron Kohnert, and Donghua Xu. Modeling defect cluster evolution in irradiated structural materials: Focus on comparing to high-resolution experimental characterization studies. *Journal of Materials Research*, 30(9):1440–1455, 003 2015.

[28] Michael P. Surh, Jess B. Sturgeon, and Wilhelm G. Wolfer. Void nucleation, growth, and coalescence in irradiated metals. *Journal of Nuclear Materials*, 378(1):86–97, 2008.

[29] Aaron A. Kohnert and Brian D. Wirth. Cluster dynamics models of irradiation damage accumulation in ferritic iron. i. trap mediated interstitial cluster diffusion. *Journal of Applied Physics*, 117(15), 2015.

[30] Donghua Xu, Brian D. Wirth, Meimei Li, and Marquis A. Kirk. Combining in situ transmission electron microscopy irradiation experiments with cluster dynamics modeling to study nanoscale defect agglomeration in structural metals. *Acta Materialia*, 60(10):4286–4302, 2012.

[31] E. Meslin, A. Barbu, L. Boulanger, B. Radiguet, P. Pareige, K. Arakawa, and C.C. Fu. Cluster-dynamics modelling of defects in -iron under cascade damage conditions. *Journal of Nuclear Materials*, 382(23):190–196, 2008. Microstructural Processes in Irradiated Materials, Proceedings of the Symposium on Microstructural Processes in Irradiated Materials, as part of the annual meeting of The Minerals, Metals & Materials Society.

[32] F. Christien and A. Barbu. Effect of self-interstitial diffusion anisotropy in electron-irradiated zirconium: A cluster dynamics modeling. *Journal of Nuclear Materials*, 346(23):272–281, 2005.

[33] M.H. Mathon, A. Barbu, F. Dunstetter, F. Maury, N. Lorenzelli, and C.H. de Novion. Experimental study and modelling of copper precipitation under electron irradiation in dilute fecu binary alloys. *Journal of Nuclear Materials*, 245(2):224–237, 1997.

[34] L. Barnard, N. Cunningham, G.R. Odette, I. Szlufarska, and D. Morgan. Thermodynamic and kinetic modeling of oxide precipitation in nanostructured ferritic alloys. *Acta Materialia*, 91:340–354, 2015.

[35] A. D. Brailsford and R. Bullough. The theory of sink strengths. *Philosophical Transactions of the Royal Society of London A: Mathematical, Physical and Engineering Sciences*, 302(1465):87–137, 1981.

[36] A.D. Brailsford, R. Bullough, and M.R. Hayns. Point defect sink strengths and void-swelling. *Journal of Nuclear Materials*, 60(3):246–256, 1976.

[37] C.H. Woo. Theory of irradiation deformation in non-cubic metals: Effects of anisotropic diffusion. *Journal of Nuclear Materials*, 159:237–256, 1988.

[38] C.S. Becquart, A. Barbu, J.L. Bocquet, M.J. Caturla, C. Domain, C.-C. Fu, S.I. Golubov, M. Hou, L. Malerba, C.J. Ortiz, A. Souidi, and R.E. Stoller. Modeling the long-term evolution of the primary damage in ferritic alloys using coarse-grained methods. *Journal of Nuclear Materials*, 406(1):39–54, 2010. FP6 IP PERFECT Project: Prediction of Irradiation Damage Effects in Reactor Components.

[39] R.E. Stoller, S.I. Golubov, C. Domain, and C.S. Becquart. Mean field rate theory and object kinetic monte carlo: A comparison of kinetic models. *Journal of Nuclear Materials*, 382(23):77–90, 2008. Microstructural Processes in Irradiated Materials, Proceedings of the Symposium on Microstructural Processes in Irradiated Materials, as part of the annual meeting of The Minerals, Metals & Materials Society.

[40] Jaime Marian and Vasily V. Bulatov. Stochastic cluster dynamics method for simulations of multispecies irradiation damage accumulation. *Journal of Nuclear Materials*, 415(1):84–95, 2011.

[41] Aaron Y. Dunn, Laurent Capolungo, Enrique Martinez, and Mohammed Cherkaoui. Spatially resolved stochastic cluster dynamics for radiation damage evolution in nanostructured metals. *Journal of Nuclear Materials*, 443(13):128–139, 2013.

[42] Aaron Dunn and Laurent Capolungo. Simulating radiation damage accumulation in -fe: A spatially resolved stochastic cluster dynamics approach. *Computational Materials Science*, 102:314–326, 2015.

[43] Y. Yamamoto, Y. Yang, K.G. Field, K. Terrani, B.A. Pint, and L.L. Snead. Letter Report Documenting Progress of Second Generation ATF FeCrAl Alloy Fabrication. Technical Report ORNL/LTR-2014/210, Oak Ridge National Laboratory, 2014.

[44] D.A. Andersson. Density functional theory calculations of the defect and fission gas properties in U-Si fuels. Technical Report Los Alamos National Laboratory, 2016.

[45] H. Shimizu. The properties and irradiation behavior of U_3Si_2. Technical Report NAA-SR-10621, Atomics International, 1965.

[46] G.L. Hofman and W.–S. Ryu. Detailed analysis of uranium silicide dispersion fuel swelling. In *Proc. of RERTR International Meeting, Berlin, Germany, September 10–13*, 1989.

[47] D.F. Sears. Development and irradiation testing of AL–U_3Si_2 fuel at Chalk River Laboratories. In *Proc. of RERTR International Meeting, Jakarta, Indonesia, November 4–7*, 1991.

[48] G.L. Hofman, Y.S. Kim, J. Rest, A.B. Robinson, and D.M. Wachs. Post-irradiation analysis of the latest high uranium density miniplate test: RERTR–8. In *Proc. of RERTR International Meeting, Washington D.C., USA, October 5–9*, 2008.

[49] J. Rest. A model for fission-gas-bubble behavior in amorphous uranium silicide compounds. *Journal of Nuclear Materials*, 325:107–117, 2004.

[50] C. A. Schneider, W. S. Rasband, and K. W. Eliceiri. NIH Image to ImageJ: 25 years of image analysis. *Nature methods*, 9:671–675, 2012.

[51] R.J. White, R.C. Corcoran, and J.P. Barnes. A Summary of Swelling Data Obtained from the AGR/Halden Ramp Test Programme. Technical Report R&T/NG/EXT/REP/0206/02, 2006.

[52] Standard Test Methods for Determining Average Grain Size. Technical Report ASTM International, Designation: E11212, 2015.

[53] C. Matthews, D.A. Andersson, and C. Unal. Radiation re-solution calculation in uranium-silicide fuels. Technical Report Los Alamos National Laboratory, 2016.

[54] M. Fell and S. M. Murphy. The nucleation and growth of gas bubbles in irradiated metals. *Journal of Nuclear Materials*, 172:1–12, 1990.

[55] C. F. Clement and M. H. Wood. *Proc. R. Soc. London*, A368:521, 1979.

[56] Kanthal APMT (Tube) Datasheet. http://kanthal.com/en/products/material-datasheets/tube/kanthal-apmt/, 2012.

[57] R. Sweet, N. George, K. Terrani, and B. Wirth. BISON fuel performance analysis of FeCrAl cladding with updated properties. Technical Report ORNL/TM-2016/475, Oak Ridge National Laboratory, 2016.

[58] J. Galloway and C. Unal. Accident-tolerant-fuel performance analysis of apmt steel clad/uo_2 fuel and apmt steel clad/un-u_3si_5 fuel concepts. *Nuclear Science and Engineering*, 182:523–537, 2016.

[59] Z. T. Thompson, K. A. Terrani, and Y. Yamamoto. Elastic Modulus Measurement of ORNL ATF FeCrAl Alloys. Technical Report ORNL/TM-2015/632, Oak Ridge National Laboratory, October 2015.

[60] K. A. Terrani, T. M. Karlsen, and Y. Yamamoto. Input correlations for irradiation creep of FeCrAl and SiC based on in–pile Halden test results. Technical Report ORNL/TM-2016/191, ORNL, May 2016.

[61] S. R. J. Saunders, H. E. Evans, M. Li, D. D. Gohil, and S. Osgerby. Oxidation growth stresses in an alumina-forming ferritic steel measured by creep deflection. *Oxidation of Metals*, 48:189–200, 1997.

[62] Y. Yamamoto, B.A. Pint, K.A. Terrani, K.G. Field, Y. Yang, and L.L. Snead. Development and property evaluation of nuclear grade wrought FeCrAl fuel cladding for light water reactors. *Journal of Nuclear Materials*, 467:703–716, 2015.

[63] B.A. Pint, K.A. Terrani, Y. Yamamoto, and L.L. Snead. Material Selection for Accident Tolerant Fuel Cladding. *Metallurgical and Materials Transactions E*, 2E:190–196, 2015.

[64] Bo Jönsson, Qin Lu, and Dilip Chandrasekaran. Oxidation and Creep Limited Lifetime of Kanthal APMT, a Dispersion Strengthened FeCrAlMo Alloy Designed for Strength and Oxidation Resistance at High Temperatures. *Oxidation of Metals*, 79:29–39, 2013.

[65] K.A. Terrani, B.A. Pint, Y.-J. Kim, K.A. Unocic, Y. Yang, C.M. Silva, H.M. Meyer III, and R.B. Rebak. Uniform corrosion of FeCrAl alloys in LWR coolant environments. *Journal of Nuclear Materials*, 479:36–47, 2016.

[66] K. A. Gamble and J. D. Hales. Preliminary Modeling of Accident Tolerant Fuel Concepts under Accident Conditions. In *TopFuel 2016*, Boise, ID, 2016.

[67] J. D. Hales, R. L. Williamson, S. R. Novascone, G. Pastore, B. W. Spencer, D. S. Stafford, K. A. Gamble, D. M. Perez, R. J. Gardner, and W. Liu. BISON theory manual: The equations behind nuclear fuel analysis. Technical report, Idaho National Laboratory, ID, USA, 2016.

[68] R. L. Williamson, K. A. Gamble, D. M. Perez, S. R. Novascone, G. Pastore, R. J. Gardner, J. D. Hales, W. Liu, and A. Mai. Validating the BISON fuel performance code to integral LWR experiments. *Nuclear Engineering and Design*, 301:232–244, 2016.

[69] B.M. Adams, L.E. Bauman, W.J. Bohnhoff, K.R. Dalbey, M.S. Ebeida, J.P. Eddy, M.S. Eldred, P.D. Hough, K.T. Hu, J.D. Jakeman, L.P. Swiler, and D.M. Vigil. Dakota, a multilevel parallel object-oriented framework for design optimization, parameter estimation, uncertainty quantification, and sensitivity analysis: Version 5.4 user's manual. Technical Report SAND2010-2183, Sandia National Laboratories, 2009, Updated April 2013.

[70] L.Y. Cheng, A. Cuadra, M. Todosow, K.A. Gamble, and P.G. Medvedev. Performance of U_3Si_2 Fuel in a Reactivity Insertion Accident. In *TopFuel 2016*, Boise, ID, 2016.

[71] U.S. Nuclear Regulatory Commission. TRACE V5.0 theory manual. Technical Report ADAMS Accession Number ML120060218, 2010.

[72] Y. Xu, T. Downar, A. Ward, T. Kozlowski, and K. Ivanov. Multi-physics coupled code reactor analysis with the U.S NRC code system TRACE/PARCS. In *PHYSOR-2006*. American Nuclear Society, 2006.

[73] IAEA. Improvement of Computer Codes Used for Fuel Behaviour Simulation (FUMEX-III): Report of a Coordinated Research Project 2008-2012. Technical Report IAEA-TECDOC-1697, International Atomic Energy Agency, 2008-2012.